



Mapping sugarcane plantation dynamics in Guangxi, China, by time series Sentinel-1, Sentinel-2 and Landsat images

Jie Wang^a, Xiangming Xiao^{a,*}, Luo Liu^b, Xiaocui Wu^a, Yuanwei Qin^a, Jean L. Steiner^c, Jinwei Dong^d

^a Department of Microbiology and Plant Biology, University of Oklahoma, Norman, OK 73019, USA

^b Guangdong Province Key Laboratory for Land Use and Consolidation, South China Agricultural University, Guangzhou 510642, China

^c Agronomy Department, Kansas State University, Manhattan, Kansas 66502, USA

^d Institute of Geographic Sciences and Natural Resources Research, Chinese Academy of Sciences, Beijing 100101, China

ARTICLE INFO

Keywords:

Agriculture
Crop mapping
Land cover
Phenology
Vegetation indices
Remote sensing

ABSTRACT

Sugarcane is a major crop for sugar and ethanol production and its area has increased substantially in tropical and subtropical regions in recent decades. Updated and accurate sugarcane maps are critical for monitoring sugarcane area and production and assessing its impacts on the society, economy and the environment. To date, no sugarcane mapping tools are available to generate annual maps of sugarcane at the field scale over large regions. In this study, we developed a pixel- and phenology-based mapping tool to produce an annual map of sugarcane at 10-m spatial resolution by analyzing time-series Landsat-7/8, Sentinel-2 and Sentinel-1 images (LC/S2/S1) during August 31, 2017 - July 1, 2019 in Guangxi province, China, which accounts for 65% of sugarcane production of China. First, we generated annual maps of croplands and other land cover types in 2018. Second, we delineated the cropping intensity (single, double and triple cropping in a year) for all cropland pixels in 2018. Third, we identified sugarcane fields in 2018 based on its phenological characteristics. The resultant 2018 sugarcane map has producer, user and overall accuracies of 88%, 96% and 96%, respectively. According to the annual sugarcane map in 2018, there was a total of 8940 km² sugarcane in Guangxi, which was ~1% higher than the estimate from the Guangxi Agricultural Statistics Report. Finally, we identified green-up dates of those sugarcane fields in 2019, which could be used to support the sugarcane planting and management activities. Our study demonstrates the potential of the pixel- and phenology-based sugarcane mapping tool (both the algorithms and the LC/S2/S1 time series images) in identifying croplands, cropping intensity and sugarcane fields in the complex landscapes with diverse crop types, fragmented crop fields and frequent cloudy weather. The resultant annual maps from this study could be used to assist farms and sugarcane mills for sustainable sugarcane production and environment.

1. Introduction

Sugarcane (*Saccharum* spp.) is a perennial crop in the grass family grown in tropical and subtropical areas (Hu et al., 2019; Sindhu et al., 2016). It accounts for about 70% of the global sugar production (Shield, 2016) and is also used as a bioenergy feedstock for ethanol production (Cardona et al., 2010; Sindhu et al., 2016). Sugarcane has been cultivated across the tropical and subtropical areas in the world (Defante et al., 2018; Sindhu et al., 2016), as it requires ample sunlight, high temperatures, and a large amount of water (Moore and Botha, 2013). The expansion of sugarcane areas in the past decades increased the demand for land, freshwater and energy resources, which raised concerns on water scarcity and environmental changes (Silertruksa and

Gheewala, 2018). Timely and accurate information of sugarcane planting area, harvested area, green-up date and harvest date is important for planning and management of the sugarcane industry, which is critical for sustainable sugarcane production, rural society, economy and environment (Mulianga et al., 2015).

To date, worldwide agricultural statistics data on sugarcane areas come from the field surveys, producer reports, questionnaires and interviews. The ground-based approach is time-consuming and labor-intensive and cannot provide timely information for all the sugarcane fields as it is based on sampling methods (Massey et al., 2017; Verma et al., 2017). Satellite remote sensing approach is a viable means for mapping crop types across local, regional and global scales and complements the ground-based statistic data (Begue et al., 2018; Sidike

* Corresponding author at: Department of Microbiology and Plant Biology, University of Oklahoma, 101 David L. Boren Blvd., Norman, OK 73019-5300, USA.
E-mail address: xiangming.xiao@ou.edu (X. Xiao).

Table 1
A summary of previous studies on sugarcane planted and harvested area mapping including classification methods, data sources at varied spatial resolutions. “Multi-source” refers to the sugarcane mapping studies using images from different satellite sensors.

Classification methods	Optical data		SAR data	Optical + SAR data
	VHSR (< 10-m)	HSR (10-m - 30-m; e.g. ASTER, SOPT-5, Landsat)	MSR (250-m - 500-m; e.g. MODIS)	Landsat, Sentinel-2, Sentinel-1 (10-m)
Visual interpretation		Aguiar et al. (2011); Rudorff et al. (2010)	Baghdadi et al. (2011)	
Images (Single-date or multi-date images) and spatial statistics of images	Verma et al., 2017	Henry et al. (2017); Hurni et al. (2014); Luciano et al. (2019); Luciano et al. (2018); Mulianga et al. (2015); Vieira et al. (2012); Vinod and Kamal (2010); Zhou et al. (2015)	Xavier et al., 2006	
Unsupervised classification (e.g. K-mean or ISODATA)				
Supervised classification (e.g. MLC, NN, DT, SVM, RF)	Verma et al. (2017)		Jiang et al. (2019a); Lin et al. (2009)	
Pixels (time series observation) and temporal statistics of pixels				This study

Note: VHSR: Very high spatial resolution; HSR: high spatial resolution; MSR: moderate spatial resolution; MLC: Maximum likelihood classifier; NN: Neural Networks; DT: Decision tree; SVM: Support vector machine; RF: Random Forest.

et al., 2019). In the last ten years, several studies have been used satellite observations to map the sugarcane fields in the world (Table 1), for example, Brazil (Aguiar et al., 2011; Luciano et al., 2019; Luciano et al., 2018; Rudorff et al., 2010; Vieira et al., 2012), China (Jiang et al., 2019a; Lin et al., 2009; Zhou et al., 2015), and India (Verma et al., 2017). These studies used optical and synthetic aperture radars (SAR) data at moderate spatial resolution (hundreds of meter), high spatial resolution (tens of meter) and very high spatial resolution (less than ten meters) (Table 1). Optical images used in those studies include the Landsat (30-m) satellite (Aguiar et al., 2011; Henry et al., 2017; Hurni et al., 2017; Johnson et al., 2014; Luciano et al., 2019; Luciano et al., 2018; Mulianga et al., 2015; Rudorff et al., 2010; Vieira et al., 2012), the Indian Remote Sensing Satellite (IRS-P6, 5.8-m) (Verma et al., 2017), the Advanced Spaceborne Thermal Emission and Reflection Radiometer (ASTER) data (15-m) (Vinod and Kamal, 2010), the Satellite Pour l’Observation de la Terre (SPOT, 10-m) (El Hajj et al., 2009) and the Moderate Resolution Imaging Spectroradiometer (MODIS, 250-m) (Rudorff et al., 2006). The SAR images used in those studies include TerraSAR-X (1-m) (Baghdadi et al., 2011), Sentinel-1 (10-m) (Jiang et al., 2019a), and ENVISAT ASAR (25-m) (Lin et al., 2009). These studies also differed from each other in terms of classification methods (Table 1), which can be grouped into three approaches: (1) visual interpretation and digitization of images, (2) spatial statistics of individual images and (3) temporal statistics of individual pixels. Most of the studies listed in Table 1 were based on the spatial statistics approach and used single- or multi-date images and calculated spatial statistics of spectral bands, vegetation indices and texture in these images, and applied unsupervised and/or supervised classification algorithms to generate sugarcane maps. As these classification methods depend on extensive training data collection, none of these studies reported annual sugarcane maps at the state and country scales. The third approach is to use time series data of individual pixels; calculate the temporal statistics of spectral bands and vegetation indices of optical data, and backscatter coefficients of SAR data in the pixels; and apply decision trees and rule-based algorithms to generate annual maps of croplands. This approach is based on the phenological characteristics of specific vegetation or crop, which are recorded in the time series image data and can be identified and used for classification of individual pixels.

A number of studies have demonstrated the potential of the phenology-based algorithms for crop mapping over multiple years across large spatial domain (Massey et al., 2017; Zhong et al., 2011; Zhong et al., 2014). This is because the phenology-based classification algorithms were developed by analyzing the crop life cycle to obtain temporal metrics of crops and generate classification rules (Bargiel, 2017; Pena-Barragan et al., 2011). The foundation of the classification rules can be from crop calendars and crop growth knowledge which are roughly consistent over years (Massey et al., 2017). These phenology-based algorithms have been successfully applied for mapping the dominant crop types, for example, paddy rice (*Oryza sativa*), soybean (*Glycine max*), maize (*Zea mays*) and winter wheat (*Triticum aestivum*) fields (Dong et al., 2015; Qiu et al., 2017; Song and Wang, 2019; Zhong et al., 2016b). As a perennial crop, sugarcane has a longer life cycle compared to the other main crops (e.g. rice, maize, soybean, and winter wheat) (Jiang et al., 2019a). There is a need to develop a new phenology-based algorithm to identify and map sugarcane fields from diverse crop types across local, state and country scales.

China is the third-largest sugarcane producer country, after Brazil and India, as reported by the United Nations Food and Agriculture Organization (FAO, <http://www.fao.org/faostat>). In China, 65% of sugarcane production occurs in Guangxi province in Southern China (Tan et al., 2007). At present, several investments from government and private companies have been made in Guangxi with an aim to increase sugarcane planting area and stalk yield. However, frequent cloud cover, multiple crop types, and small, fragmented fields in Guangxi pose challenges for remote sensing applications in this region (Chen et al.,

2011; Li et al., 2014). Considering the potential limitations of remote sensing in sugarcane crop mapping and the actual demands of farmers, sugar mills and local government for timely and accurate information on sugarcane plantations, we proposed three objectives in this study: (1) to develop a pixel- and phenology-based algorithm to extract crop phenology metrics for sugarcane field mapping at 10-m resolution using Landsat-7/8, Sentinel-2, and Sentinel-1 time-series images; (2) to examine the critical phenology metrics of sugarcane, such as green-up dates (or start of the season, SOS) and senescent dates (or end of the season, EOS), to produce an annual map of sugarcane fields in Guangxi province in 2018; and (3) to monitor the green-up dates of the sugarcane fields in 2019 to quantify how many sugarcane fields in 2018 continued to be cultivated as sugarcane in 2019, which is important for the planting management of sugarcane crops. We proposed to combine time series Landsat (30-m, 16-day revisit cycle), Sentinel-2A/B (10-m, 5-day revisit cycle), and Sentinel-1A/B, 10-m, 6-day revisit cycle). The sugarcane mapping platform and resultant data products can be used by different stakeholders, including local government agencies, farmers, sugar mills, and insurance companies, for management and monitoring of sugarcane plantations and sugar production.

2. Materials and methods

2.1. Study area

Guangxi Autonomous Region in Southern China consists of 14 prefecture and cities with a total land area of ~236,700 km² (Fig. 1). It has the subtropical to tropical climate. The mean annual air temperature was 20 °C and mean annual precipitation was 1800 mm during 2000–2019 for the entire Guangxi (Fig. S1). The topography is complex, including mountains, hills and plains, and elevation ranges from 0 to 2800-m above sea level (Fig. 1b). The central and southern parts are mostly flat plains but surrounded by mountains and hills. Diverse crops are cultivated in the low hills and plains regions. According to the Guangxi Statistical Yearbook in 2018, rice, sugarcane and maize are the dominate crop types, which accounts for about 32%, 15% and 10% of the total crop planted area, respectively (Fig. S2).

Sugarcane is the largest cash crop in Guangxi and its area was ~10,000 km² in recent years (Zhang et al., 2015; Tan et al., 2007). Its growing period in Guangxi ranges from 8 months to more than one year (Wang et al., 2014; Tan et al., 2007). The life cycle of sugarcane differs

from annual crops such as rice and maize (Tan et al., 2007). Sugarcane has four major growing stages (Fig. 2): (1) ratoon germination or planting, (2) tillering, (3) rapid growth, (4) maturity and harvest (Fig. 2) (Lin et al., 2009). The ratoon germination of sugarcane occurs between late January and late March. New sugarcane planting period usually occurs between late March and early May. The tillering period starts usually in May and lasts about one-month. Sugarcane starts to elongate the stem and grow rapidly between June and October. In November, sugarcane crops are mature and ready to be harvested. Sugarcane harvest started in November and continued into April of next year, which ensures the continuous supply of fresh sugarcane stalks for cane sugar production at the sugar mills over time.

Rice and maize are the other two dominant crop types in Guangxi (Fig. S2). There are single and double rice cropping systems (Fig. 2) (Jiang et al., 2019b). Single rice is usually planted in late May and harvested in early October. Double rice consists of early and late rice. Early rice is usually grown from late March to late July. Late rice is planted in the same field as early rice and grows from late July to late October. Between the early and late rice cycles, there is a short time window in middle and late July for rush-harvesting of early rice and rush-transplanting of late rice, namely, “Shuangqiang” (Fig. 2). Maize is a dryland crop and the cultivation practices are diverse in Guangxi. Spring maize is cultivated from middle February to late June, and summer maize is cultivated from early July to the late November (Fig. 2) (Meng, 2006). The different cropping cycles among these major crops provide the foundation for developing the phenology-based algorithms to identify and map the sugarcane fields in this study (see more detail in Section 2.3).

2.2. Datasets

2.2.1. Landsat and Sentinel-2 data

In this study, we collected the top of atmosphere (TOA) reflectance data of Landsat-7/8 and Sentinel-2 (LC/S2) from August 31, 2017 to July 1, 2019, as Sentinel-2 surface reflectance (SR) data (Level-2A) for the study area over the entire study period were not available at the Google Earth Engine (GEE) platform when we first carried out this study in 2019. While the TOA data have significant limitations given their sensitivity to changes in the composition of the atmosphere through time, they are still useful for exploiting the spectral differences among crops within each specific data, which are essential for cropland

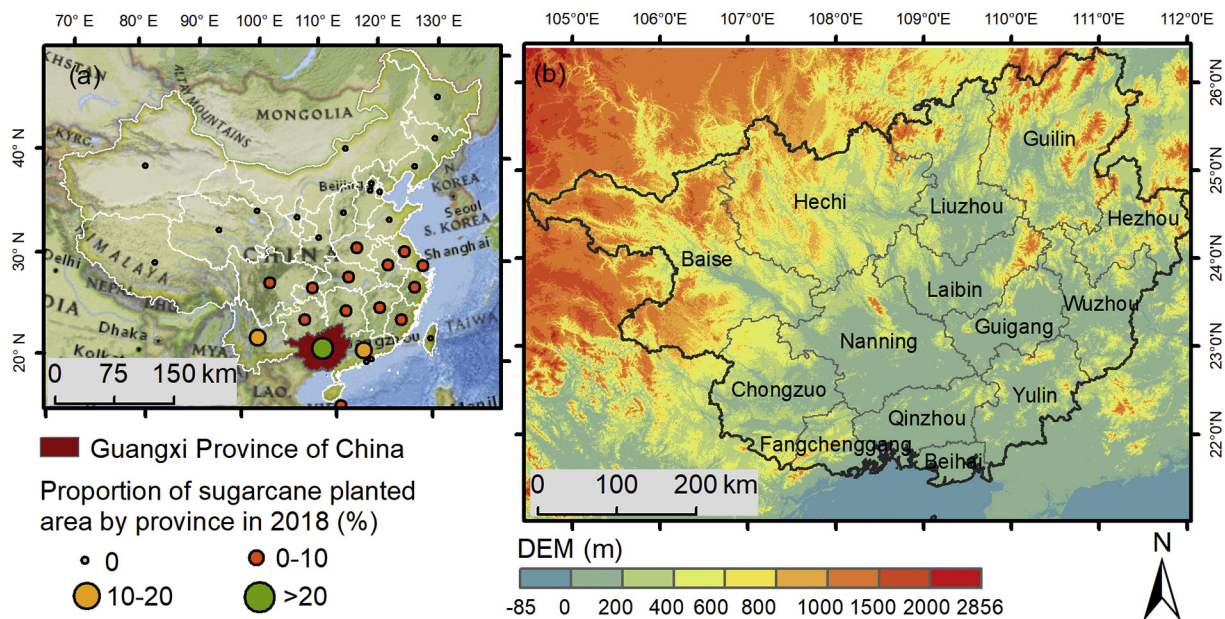


Fig. 1. (a) Location and (b) topography of Guangxi province, China. It is the largest sugarcane production base of China which is selected as the study area.

Crops	Year i-1		Year i												Year i+1			
	11	12	1	2	3	4	5	6	7	8	9	10	11	12	1	2	3	4
SC	Mature and Harvest		Ratoon germination			Planting	Tillering	Rapid growth					Mature and Harvest		Ratoon germination			Planting
			Harvest								Harvest							
RC			Early rice				H	Late rice									Early rice	
								S	Single Rice									
MZ			Spring maize						Summer maize							Spring maize		

Fig. 2. Crop calendars for the major crops in Guangxi including sugarcane (SC), rice (RC), and maize (MZ). This figure shows the crop phenology stages which start in the former November (11) and cross the next entire year and end in the following April (4). In this figure, ‘H’ and ‘S’ denote harvest and sowing separately. Year i-1, Year i, and Year i + 1 present three consecutive years.

classification (Jin et al., 2019). Landsat data included all available standard Level-1 Landsat-7 Enhanced Thematic Mapper (ETM+) and Landsat-8 Operational Land Imager (OLI) from the United States Geological Survey (USGS). Landsat-7/8 have 30-m spatial resolution and 16-day temporal resolution. Sentinel-2 Multi Spectral Instrument (MSI) data included all available Level-1C Sentinel-2A and Sentinel-2B images from the European Space Agency (ESA). Sentinel-2A/B data together have 10-m spatial resolution and 5-day temporal resolution. The pre-processing of LC/S2 data cube includes four main steps: identifying bad-quality observations, combining Landsat-7/8 and Sentinel-2 TOA data, calculating vegetation indices (VIs), and constructing LC/S2 VIs time series.

The quality of Landsat TOA data was identified by the CFmask which is included in the corresponding Landsat surface reflectance data (Zhu and Woodcock, 2012). Observations without clouds, cloud shadows, snow/ice and scan-line corrector (SLC)-off gaps were used as good-quality observations. The quality of Sentinel-2 data was assessed based on the quality band in the metadata, which identifies those observations having cirrus and opaque clouds as bad-quality observations and stored as NODATA in the image files. Fig. S3 shows the spatial distributions of number of observations and number of good-quality observations (GOBs) in a pixel in Guangxi from the combined LC/S2 TOA datasets.

There are some differences in band wavelengths and spectral reflectance among ETM+, OLI and MSI sensors (Roy et al., 2016; Zhang et al., 2018). Therefore, it was necessary to harmonize the band reflectance values from different sensors in order to use these data together and construct a comparable time series (Roy et al., 2016; Zhang et al., 2018). There are a number of ways to do it (Griffiths et al., 2019; Shao et al., 2019), and we used the approach of ordinary least squares (OLS) regression, proposed by Roy et al. (2016) and Zhang et al. (2018). We transferred the spectral bands of Landsat-7 ETM+ and Sentinel-2 MSI to match the observations of Landsat-8 OLI, which was used as a reference.

Spectral indices that are sensitive to vegetation greenness and water status can be used to capture the physical differences of land cover types (Di Vittorio and Georgakakos, 2018) and characterize the growth curves of individual crop types (Jackson et al., 2004; Wardlow et al., 2007). Normalized Difference Vegetation Index (NDVI, Eq. 1) (Tucker, 1979) and Enhanced Vegetation Index (EVI, Eq. 2) (Huete et al., 2002) are highly related to leaf area index and chlorophyll in the canopy and widely used to indicate the vegetation greenness. Land Surface Water Index (LSWI, Eq. 3) (Xiao et al., 2005) is sensitive to the land surface moisture from both vegetation and soils. Modified Normalized

Difference Water Index (mNDWI, Eq. 4) was developed to delineate open surface water body by suppressing background information from vegetation and soils (Xu, 2006). The four spectral indices were calculated from the blue, green, red, near infrared (NIR) and shortwave infrared (SWIR) spectral bands based on the time series TOA data from Landsat-7/8 and Sentinel-2 (Eq. 1–4).

$$NDVI = \frac{\rho_{NIR} - \rho_{Red}}{\rho_{NIR} + \rho_{Red}} \tag{1}$$

$$EVI = 2.5 \times \frac{\rho_{NIR} - \rho_{Red}}{\rho_{NIR} + 6 \times \rho_{Red} - 7.5 \times \rho_{Blue} + 1} \tag{2}$$

$$LSWI = \frac{\rho_{NIR} - \rho_{SWIR}}{\rho_{NIR} + \rho_{SWIR}} \tag{3}$$

$$mNDWI = \frac{\rho_{Green} - \rho_{SWIR}}{\rho_{Green} + \rho_{SWIR}} \tag{4}$$

Image compositing is an approach to construct time series data at a regular interval, which can reduce the influence of clouds and uneven observations in time (Griffiths et al., 2019). We composited the spectral index data from LC/S2 to construct the time series VIs data at a 10-day interval, using the same approach as a recent study (Liu et al., 2020). When there were multiple good-quality observations within a 10-day period, we calculated the mean value of all the observations and used it to represent the observation value of the 10-day period. When there was no good-quality observation in a 10-day period, we filled the data gap by the linear interpolation method, which used the adjacent good-quality observations in the time series (Liu et al., 2020). For phenology analysis, we further smoothed the NDVI times series by the Savitzky-Golay filter to eliminate small fluctuations using a moving window of size 9 and a filter order of 2 (Chen et al., 2018b; Fischer et al., 2001). As LSWI is sensitive to vegetation water and soil moisture that are affected by rainfall and snow, the LSWI time series data was not smoothed for phenology analysis.

2.2.2. Sentinel-1 data

The SAR images from the European Space Agency (ESA) Sentinel-1A and Sentinel-1B were used in this study. We used the GEE platform to process all 10-m Sentinel-1 data with VH polarization band for the study area from August 2017 to July 2019. The VH time series data were built with a 12-day interval using the linear interpolation method to match the revisit time of Sentinel-1. The noise of the VH time series was smoothed using a moving average method with a moving window of size 3.

2.2.3. Ground reference data

The ground data of individual crop types are critical for developing the training and validation samples to support image analysis for mapping crop types. Field work was conducted to collect geo-referenced field photos on different crop types in two test areas in December 2018 (Fig. S4). These field photos include the dominant crop types such as sugarcane, paddy rice, maize and tubers, which have been released to the public by the Global Geo-Referenced Field Photo Library at the University of Oklahoma (OU) (<http://www.eomf.ou.edu/photos>). According to these field photos and the very high spatial resolution images at Google Earth, we collected training samples for sugarcane (124 polygons) and non-sugarcane crops (129 polygons), respectively (Fig. S4).

In addition, we collected the sugarcane field size information in two pilot study regions in 2018 by visual interpretation of the multi-spectral images acquired by a small unmanned aerial system (sUAS) (Fig. S5). A total of 2388 sugarcane fields were delineated by local professionals and digitized as polygons. We inferred the sizes of these polygons as sugarcane field sizes (Fig. S6). The mean and median values of sugarcane fields are 2488 m² and 1299 m², respectively (Fig. S6). Out of the 2388 sugarcane fields, approximately 2% are less than 100-m², 32% are less than 900-m², and only 5% are larger than 10,000-m² (Fig. S6). These polygons were used to estimate the potential and limit of using LC/S2 integrated data to identify the sugarcane crop at varying field sizes.

2.2.4. Sugarcane area data from agricultural statistics reports

Guangxi Bureau of Statistics publishes annual reports on the planting areas of the main crops in each prefecture and city (<http://tjj.gxzf.gov.cn/tjsj/tjnj/>). We acquired the 2019 statistical yearbook that reports the sugarcane planting area in 2018 at the prefecture and city level. This dataset was used to compare with the resultant LC/S2-based sugarcane map at the prefecture and city level.

2.3. Methods

Fig. 3 shows the workflow to produce the annual map of sugarcane fields in 2018. We first identified the croplands and other land cover types and then delineated sugarcane fields within the cropland layer using LC/S2 NDVI and LSWI time-series data (Fig. 3). After these classification processes, we monitored the seasonal dynamics of sugarcane fields in the following year and produced a green-up date map of sugarcane fields in 2019. In the following paragraphs, we described various steps in the workflow.

2.3.1. Annual maps of croplands and other land cover types in 2018

In this study, we grouped land cover types into four categories: water-related land cover type, non-vegetated land, evergreen vegetation, and croplands. Water-related land cover types include open surface water bodies, natural wetlands, paddy rice fields, and flooded lands. The non-vegetated land are built-up surfaces and barren land. In previous studies, we developed pixel- and phenology-based algorithms to map surface water bodies (Zou et al., 2018), paddy rice (Dong et al., 2015; Zhang et al., 2017), forests (Qin et al., 2017b), built-up and barren lands (Qin et al., 2017a). Here, we systematically studied the seasonal dynamics of NDVI and LSWI data from LC/S2, and VH backscatter data from Sentinel-1 for the major croplands (sugarcane, paddy rice, and maize), and other land cover types (forests, built-up and barren land, and water bodies) in the study area (Fig. 4, Fig. S7). Based on the signature analysis in this study and some previous work, we generated annual maps of evergreen vegetation, built-up and barren land, and water-related land cover types in 2018, which serve as masks. We assigned the remaining pixels that are not classified as one of the three masks to be croplands, which are used for further analysis (see Section 2.3.2). The mapping algorithms were described in the following paragraphs and summarized in Table 2.

Evergreen vegetation, including forests, tree plantations, orchards and shrubs, are evergreen plants with high NDVI and LSWI throughout the year (Fig. 4d, Fig. S7). In our previous studies, we developed a decision tree classification algorithm that uses LSWI and EVI time series data to identify evergreen vegetation (more than 90% observations with LSWI > 0 in a year and minimum EVI > 0.2). The algorithm was applied with MODIS and Landsat data for evergreen vegetation mapping in China, USA, and the pan-tropical zones (Dong et al., 2015; Qin et al., 2019; Wang et al., 2018a; Xiao et al., 2009). In this study, we used the same algorithm to produce the evergreen vegetation map in Guangxi.

The built-up surfaces and barren lands usually have higher reflectance in SWIR band than in NIR band, which results in a negative LSWI (LSWI < 0), and we developed an algorithm that uses LSWI time series data to identify built-up and barren lands (more than 90% observation with LSWI < 0 in a year) (Dong et al., 2015). Spectral data analysis in this study also show low NDVI and LSWI for built-up and barren lands (Fig. 4f, Fig. S7). We used the same algorithm to generate the built-up and barren land mask. Given very complex and fragmented landscapes in Guangxi, we modified the threshold of LSWI from 0 in Dong et al. (2015) to 0.2 (LSWI < 0.2) to identify those mixed pixels of built-up/barren land and vegetation (Fig. 4f).

Water-related land cover types are diverse and dynamics. We developed an algorithm that uses time series spectral indices (NDVI, EVI, mNDWI) to identify surface water, which is expressed as (mNDWI > NDVI or mNDWI > EVI) and (NDVI < 0.1 or EVI < 0.1) (Zou et al., 2018). Year-long surface water bodies are those pixels that have ≥ 75% observations identified as surface water in a year. Seasonal surface water bodies are those pixels that have ≥ 5% observations identified as surface water in a year. In addition, paddy rice fields have a seasonal flooding (water) signal, i.e. the mixed feature of water and plants, during the flooding and transplanting period (Xiao et al., 2006; Xiao et al., 2005). This unique plant/water feature often lasts several weeks (about one month). For the double paddy rice fields in the southern China, this period is about two weeks. A challenge for paddy rice mapping using optical satellites is to have sufficient number of good-quality observations to capture this flooding signal during the short time window (Dong et al., 2015). In this study, we used the Sentinel-1 VH backscatter data. VH backscatters are very low (VH < -20) for the water covered pixels (Fig. 4b, e, Fig. S7). Therefore, we generated another wetland mask to reduce the uncertainty from optical satellite observations using the algorithm of NDVI > 0.3, LSWI > 0 and VH < -20 during the rush-harvesting and rush-transplanting period.

2.3.2. Annual map of cropping intensity (single-, double- and triple-cropping croplands) in 2018

For those pixels that are classified as upland croplands (see section 2.3.1), we further identified them as single-, double- or triple-cropping croplands. The NDVI temporal profile analysis is widely used to identify the cropping intensity patterns (Chen et al., 2018b; Gao et al., 2017; Jonsson and Eklundh, 2004). NDVI increases from green-up stage and reaches the maximum during the peak growing stage. After the crop matures, NDVI is reduced until the crop is harvested. Meanwhile, bare soils and crop residuals after crop harvest usually have very low values of LSWI, which can be employed as the crop harvest signals (Chen et al., 2018a). Therefore, in this study, we used the NDVI time-series smoothed by SG filter and the LSWI time-series as inputs to identify the phenology metrics of start, peak, and end of the crop growth cycles for individual pixels.

This analysis can be summarized as three steps. First, we used a peak finding method to flag the potential peaks and troughs along the NDVI profiles (Li et al., 2014). A peak is defined as the time with NDVI value higher than the previous and the following values, while a trough is defined as the opposite case. Croplands generally have high peak values in NDVI that can exceed 0.5 (Defries and Townshend, 1994; Galford et al., 2008; Liu et al., 2020). This condition was used to

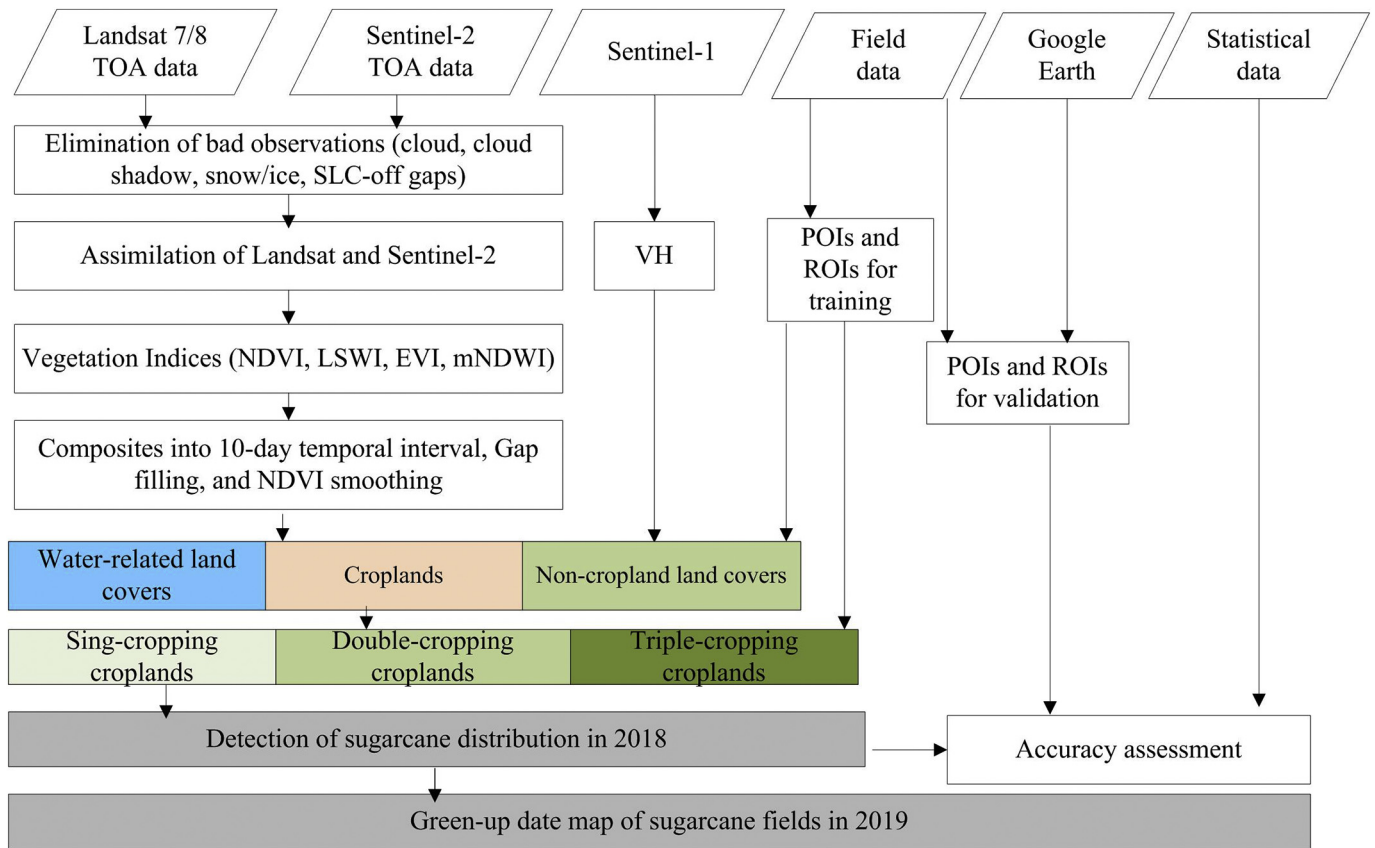


Fig. 3. The workflow for identifying and mapping sugarcane fields by time series Landsat and Sentinel-2 data. It includes data preprocessing, cropland mapping, cropping intensity analysis, sugarcane field map in 2018, green-up date map of sugarcane fields in 2019, and accuracy assessment of sugarcane field map in 2018. (For interpretation of the references to colour in this figure legend, the reader is referred to the web version of this article.)

exclude the spurious peaks.

Second, we flag the potential troughs between two successive peaks. If the bare soil signals were detected, these two continuous peaks are divided into two cropping cycles. Here, bare soils were detected by using LSWI less than a threshold. Previous studies show that the LSWI of bare soils vary between 0 and 0.2, depending on the soil moisture content from the northern to the southern China (Chen et al., 2018a; Dong et al., 2015). Therefore, we used a dynamic LSWI threshold (T_{LSWI}) calculated by the eqs. 5 and 6 to separate the cropping intensity in this study (Liu et al., 2020).

$$T_p = LSWI_{min} + (LSWI_{max} - LSWI_{min}) \times 0.15 \quad (5)$$

$$T_{LSWI} = \begin{cases} 0, & T_p < 0 \\ T_p, & 0 \leq T_p \leq 0.2 \\ 0.2, & T_p > 0.2 \end{cases} \quad (6)$$

where T_p is the potential LSWI threshold, and T_{LSWI} is the final LSWI threshold that is used to identify the bare soil signals. $LSWI_{min}$ and $LSWI_{max}$ are the minimum and maximum LSWI values during the entire study period.

Finally, we calculated the peak number in 2018 to generate an annual map of single- (with one peak), double- (with two peaks), and triple- (with three peaks) cropping croplands in 2018. This method was used because the number of peaks in a year is an indicator to classify the cropping system (Chen et al., 2018b).

2.3.3. Annual map of sugarcane fields in 2018

Sugarcane is one of the upland crops that have single cropping cycle in a year. The growing season of sugarcane is longer than other major crops (i.e. paddy rice, maize) in Guangxi (Fig. 2, Fig. 4). Additionally, sugarcane was planted by cuttings not seeds, which could lead to a

different green-up speed (GUS) from other crops at the beginning of the growing season. According to these unique characteristics of sugarcane, we extracted the critical phenology metrics, including the green-up date (GUD, or start of the season), senescent date (SD, or end of the season), growing-season length (GSL), start date of peak season (SDPS), and green-up speed (GUS). These metrics were defined by using the commonly used algorithms and NDVI time series (Jonsson and Eklundh, 2004; Wang et al., 2018b). GUD and SDPS are respectively defined as the times of NDVI reaching 10% and 90% of the NDVI amplitude from the left minimum. SD is the time of NDVI having 10% amplitude higher than the right minimum. The GSL represents the days between green-up date and senescent date. The GUS is defined as the ratio of the NDVI change over the number of days between GUD and SDPS. Fig. 5a shows the detailed information of the phenology metrics.

The training samples of sugarcane and other crops were overlaid with the five phenology metric layers to carry out a signature analysis. The results showed that the GUD of sugarcane occur mostly in late January to late April, in other words, day of year (DOY) from 20 to 110 in 2018. SDPS is in early May to middle August (DOY from 120 to 230), and SD starts early November with DOY larger than 310. The GUS mainly gathers between 0.002 and 0.007. GSL of sugarcane crops are mostly larger than 240 days.

Based on the results of signature analysis, we developed a decision classification approach of $20 < GUD < 110$ & $120 < SDPS < 230$ & $SD > 310$ & $0.002 < GUS < 0.007$. This approach was implemented to identify sugarcane fields among the dryland cropland pixels with a single cropping cycle system, which are the result from the analysis in Section 2.3.1 and 2.3.2.

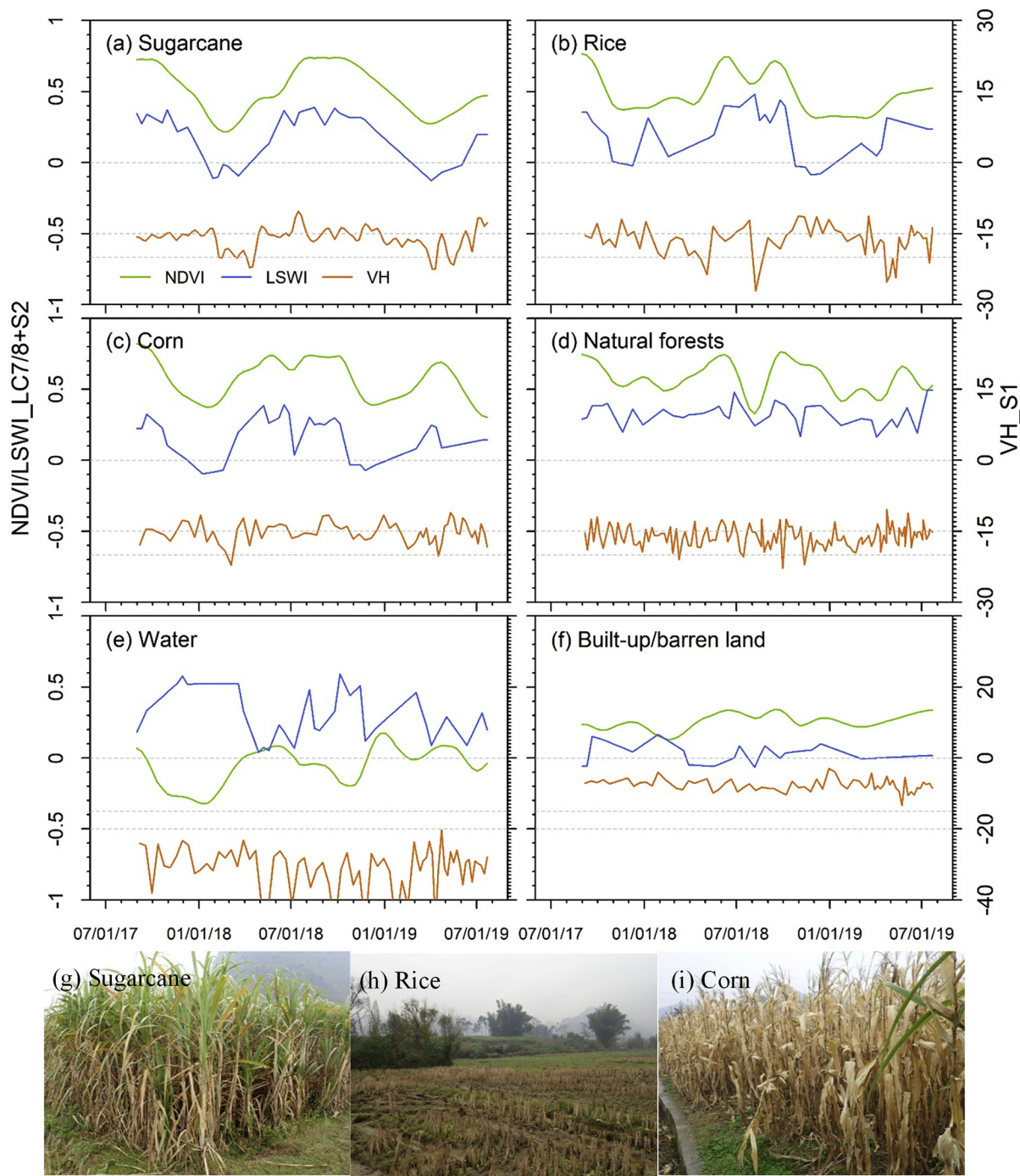


Fig. 4. Seasonal dynamics of Landsat/Sentinel-2-based NDVI, LSWI, and Sentinel-1 VH for sugarcane, rice, corn, natural forests, water, and built-up/ barren land. (g, h, i) shows the field photos for sugarcane, rice, and corn crops taken in December 2018.

Table 2

A summary of the phenology-based algorithms to generate the main non-cropland land cover types in the study area. They were used as the mask layers to produce the potential cropland distribution in this study.

Land cover types	Algorithms	References
Evergreen vegetation	LSWI > 0 and EVI > 0.2, Freq > 90%	Xiao et al., 2009, Dong et al., 2015
Built-up and barren land	LSWI < 0.2, Freq > 90%	Dong et al., 2015
Water-related land covers	Permanent water body (mNDWI > NDVI or mNDWI > EVI) and (NDVI < 0.1 or EVI < 0.1), Freq > 75% Seasonal water body including paddy rice fields (mNDWI > NDVI or mNDWI > EVI) and (NDVI < 0.1 or EVI < 0.1), Freq > 5%; NDVI > 0.3 and LSWI > 0 and VH < -20 within the flooding and transplanting period	Zou et al., 2018

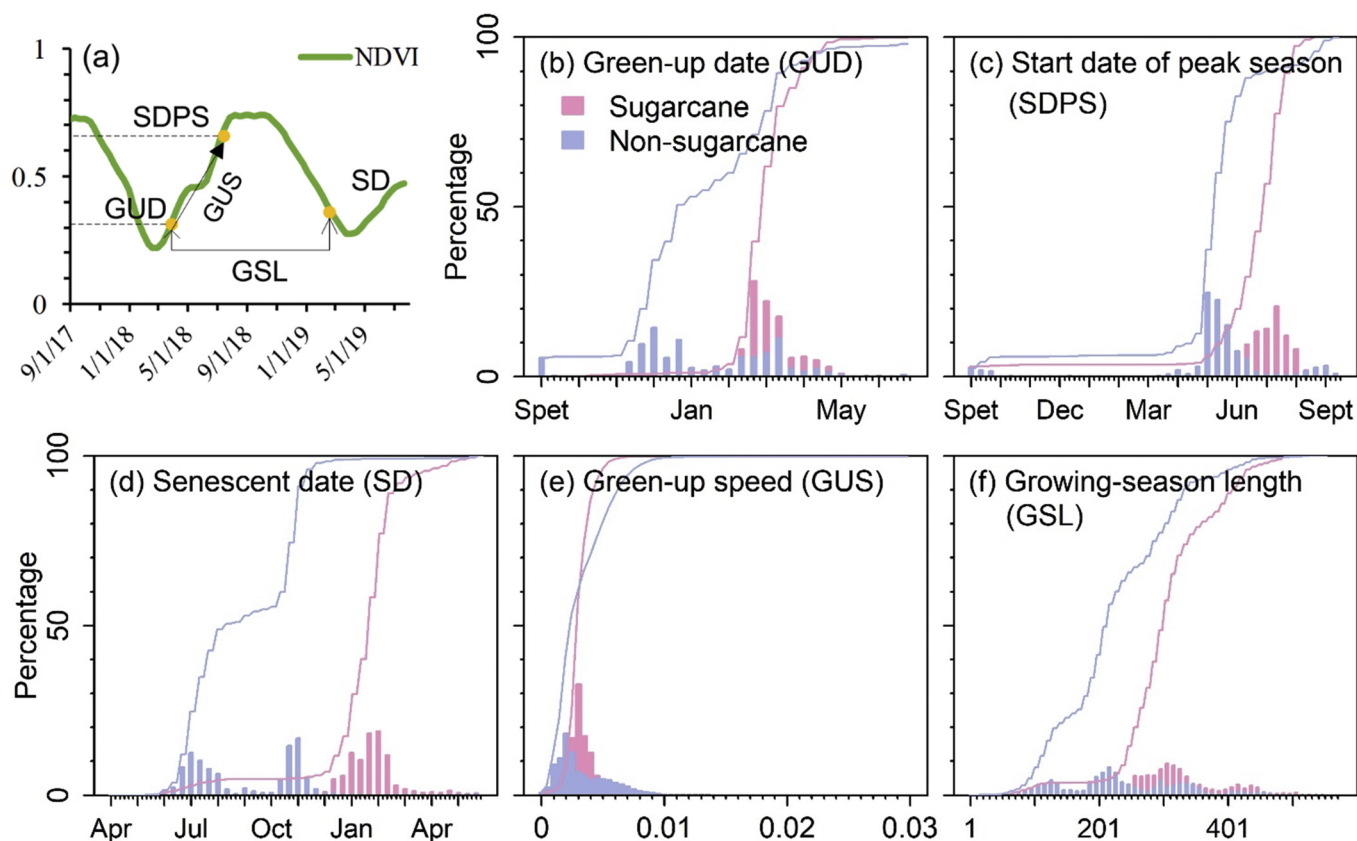


Fig. 5. (a) An NDVI temporal profile for the sugarcane crop is shown from 09/01/2017 to 07/01/2019. Some of phenological parameters are presented based on the NDVI curve, including green-up date (GUD, left 10% level), start date of peak season (SDPS, left 90% level), senescent date (SD, right 10% level), green-up speed (GUS, slope from green up to start of peak season), and the growing-season length (GSL). (b-f) signature analysis of sugarcane and non-sugarcane crops at each phenology parameter layer using the histogram statistics method. The training samples for sugarcane and non-sugarcane crops used in this analysis are shown in Fig. S4. (For interpretation of the references to colour in this figure legend, the reader is referred to the web version of this article.)

2.3.4. Accuracy assessment of the resultant annual maps and area comparison

We collected the ground reference data in 2018 using the stratified random sampling method for the accuracy assessment based on multiple information sources (Olofsson et al., 2014). We used the national land-use land cover map of China in 2015 as a basis to generate four stratum of croplands, forests, built-up and barren lands, and surface water body in Guangxi province. Within the cropland layer, we generated random points and their square buffers at a distance of 30-m. This 30-m distance is to match the Landsat and Sentinel-2 spatial resolutions and crop field size in the study area. Then, we visually selected the sugarcane and non-sugarcane samples by overlaying these random square buffers with the very high spatial resolution images in Google Earth and Sentinel-2 images in 2018. Meanwhile, the ground field photos in the test area were used as an auxiliary reference in the visual procedure. Finally, total numbers of validation samples we collected are 203 polygons (8033 pixels) for sugarcane fields and 762 polygons (30,175 pixels) for non-sugarcane cropland fields (Fig. S8). These validation samples were used to assess the accuracy of the sugarcane map in 2018 by calculating the confusion matrix following the best practices method (Olofsson et al., 2014).

We also calculated the sugarcane planted areas from the 2018 sugarcane map for all prefectures and cities in Guangxi. The results were compared with the statistics data of sugarcane planted area reported by Guangxi Bureau of Statistics for 2018. This cross-comparison is to evaluate the agreements between the remote sensing approach and the agricultural statistics approach at prefecture and city level.

2.3.5. Monitoring green-up dates of sugarcane fields in 2019

After generating the 2018 sugarcane distribution map through the processes described from Section 2.3.1 to 2.3.3, we continued to identify and monitor the green-up dates of the sugarcane fields in 2019. This effort aims to provide near-real-time information for the local government and stakeholders on the temporal dynamics of sugarcane fields, which can be used for managing sugarcane planted area. The green-up dates of sugarcane fields in 2019 was estimated by using the same approach based on the smoothed NDVI and LSWI time series, as described in Section 2.3.3.

3. Results

3.1. Annual maps of croplands and other land-cover types in 2018

Fig. 6 shows the high-level land cover types across Guangxi, China, in 2018 including water-related land covers, built-up and barren lands (non-vegetated land), evergreen vegetation, and croplands. Evergreen vegetation is the largest land cover type, which is followed by croplands, built-up and barren lands, and water-related land cover types. The layers of evergreen vegetation, built-up and barren lands, and water-related land covers were further applied as masks and the map of croplands is produced by removing those non-crop pixels. The croplands are distributed unevenly in the region, predominately being located in the south. This cropland distribution map has been used as an input for mapping crop intensity in 2018.

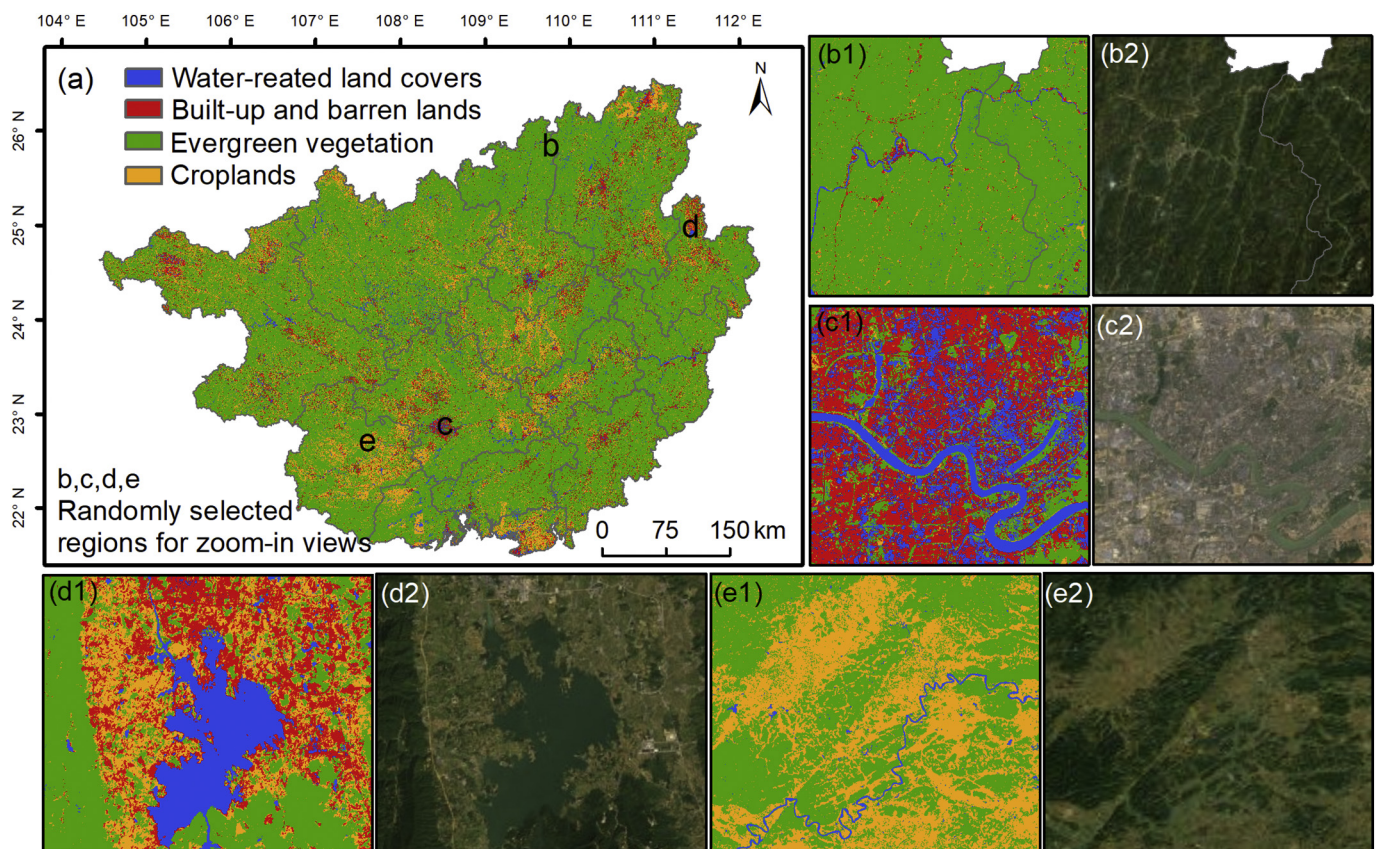


Fig. 6. (a) Distribution of water-related land covers, built-up and barren lands, evergreen vegetation, and potential croplands in Guangxi, China. Four regions, denoted as b, c, d, e in Figure a, were selected randomly. The zoom-in views in Figure a for the four regions are shown in Figure b1, c1, d1, e1 and the very-high-resolution views from Google Earth are shown in Figures b2, c2, d2 and e2.

3.2. Annual map of single-, double- and triple-cropping croplands in 2018

As described in Section 2.3.2, we identified the peak numbers in 2018 over the cropland pixels by analyzing the LC/S2 NDVI time series during September 2017 to July 2019. The annual map of cropping intensity in 2018 was produced (Fig. 7). This map shows the spatial distribution of single-, double- and triple-cropping croplands in Guangxi. Single cropland accounts for about 71% of the total cropland area, followed by double (20%) and triple (2%) croplands. In ~7% of the potential cropland areas, the algorithm was not able to identify a cropping cycle, and they are assigned to “No cycle”. Only those croplands with a single cropping cycle is used as input for mapping sugarcane fields.

3.3. Annual maps of sugarcane fields and associated phenology metrics in 2018

For those pixels identified as single-cropping cropland in 2018, we identified their phenology variables using the time series analysis approach (Section 2.3.3) (Fig. 8). Using the four phenology variables (green-up date, senescent date, start date of peak season, green-up speed) as inputs, we identified sugarcane fields in 2018 by the decision classification algorithms proposed in this study. The resultant annual map of sugarcane fields at 10-m spatial resolution show that sugarcane fields are concentrated in a few prefecture and cities, e.g., Chongzuo, Nanning and Laibin (Fig. 8).

We summed the sugarcane areas by prefecture and city from the sugarcane map in 2018 and compared them with the sugarcane planting area in 2018 from the 2019 statistical yearbook (Fig. 9a). There is a significant linear relationship (slope = 0.93, $R^2 = 0.95$, $P < .001$) between the sugarcane areas derived from our results and

those from the statistical reports (Fig. 9b). The total area of sugarcane fields in Guangxi from the 2018 sugarcane map is 8940 km², which is only 0.85% higher than the area estimate (8864 km²) from the agricultural statistics report.

3.4. Accuracy assessment for the 2018 sugarcane map

The accuracy of the sugarcane distribution map in 2018 was evaluated using the validation samples described in Section 2.3.4 (Fig. S8). By overlaying the validation samples and the resultant map, we calculated the confusion matrix (Table 3). The overall, user, and producer accuracies are 0.96 ± 0.002 , 0.96 ± 0.005 , and 0.88 ± 0.007 , respectively.

We used the detailed maps of sugarcane fields (polygons) derived from sUAS images in two small pilot study regions (Fig. S5, Fig. 10a, d) to quantitatively evaluate the omission errors of our sugarcane map at changing sugarcane field sizes (Fig. 10). For each sugarcane polygon, we separately identified the pixels recognized or not by the resultant sugarcane map (Fig. 10c, e). The statistical results showed the proportions of unrecognized pixels were usually lower than 20% along with the changes of sugarcane field sizes (Fig. 10f). In comparison, the small field parcels less than 400-m² had a slightly higher proportions of unrecognized pixels (about 14%) than those fields larger than 400-m² (about 10%) (Fig. 10f).

3.5. Green-up date map of sugarcane fields in 2019

Local governments and sugar mills pay close attention to the green-up date of sugarcane fields in spring as it is an indicator for sugarcane planted area and can be used to assist farmers for their management activities. We used the sugarcane distribution map in 2018 as the base

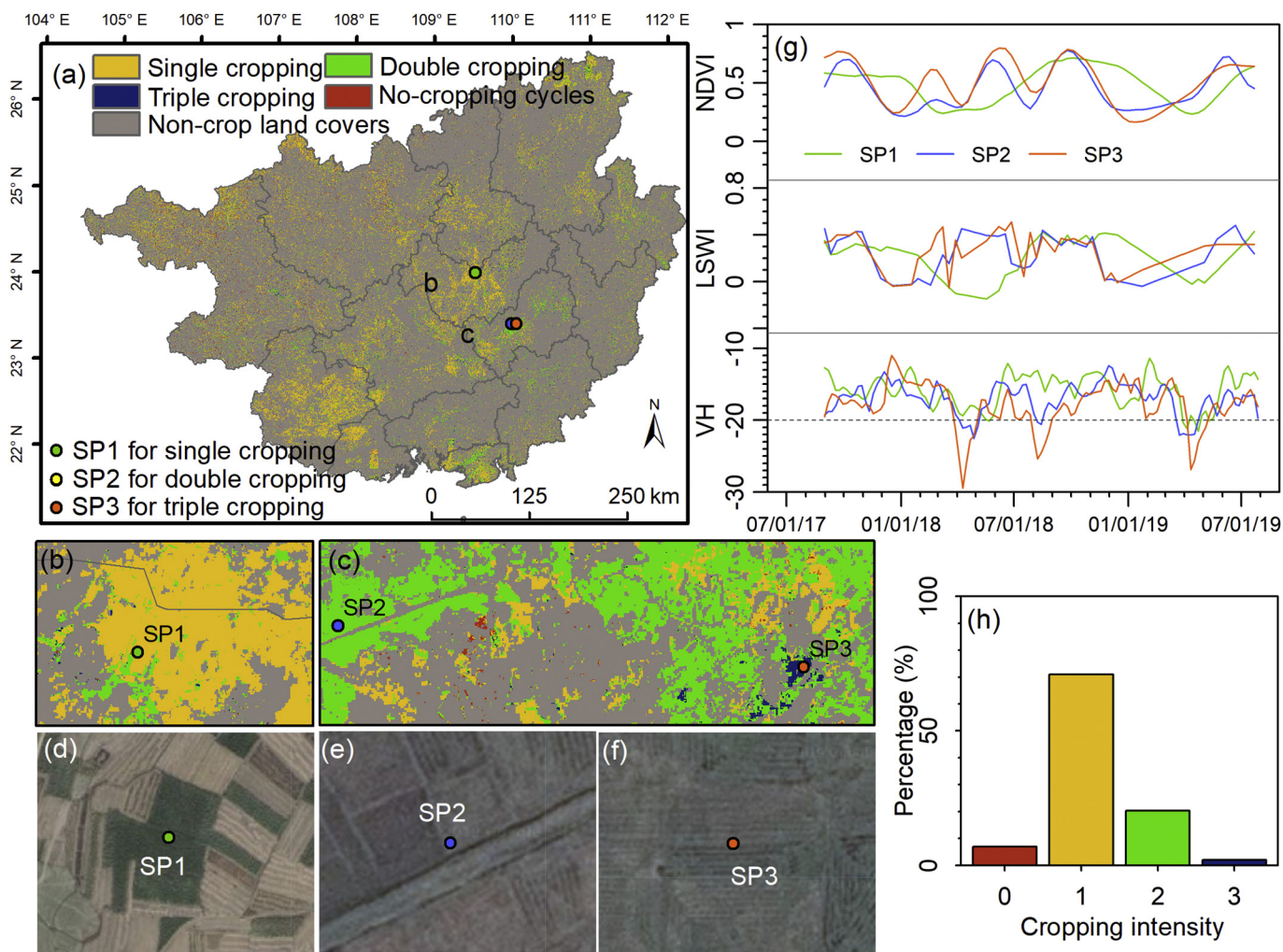


Fig. 7. Annual map of cropping intensity in Guangxi, China in 2018. (a) Spatial distribution of single, double- and triple- cropping croplands in Guangxi, China. Three sample areas were selected as SP1, SP2, and SP3 to show the zoom-in views (b, c) in the resultant map, (d, e, f) the landscapes from Google Earth images, and (g) the temporal profiles of NDVI, LSWI and VH for sing-, double- and triple- cropping croplands, respectively. (h) the proportions of no cropping cycle (0), single- (1), double- (2) and triple- (3) cropping croplands over the potential croplands in Guangxi, China during 2018.

map and identified when these sugarcane fields started to green-up during 12/2018–6/2019 by analyzing the LC/S2 NDVI and LSWI time series data in 2018/2019. Fig. 11a shows the spatial distribution of green-up date (displayed in month) of sugarcane fields in 2019. The green-up dates (months) range from December 2018 to June 2019. Approximately 10% of the sugarcane fields started to green up in February 2019, 62% in March and April, and 11% in May (Fig. 11b). In about 8% of the sugarcane fields in 2018, the algorithm has not detected the green-up signal in the sugarcane planting period of 2019, which indicates that these fields may not be cultivated for sugarcane in 2019.

4. Discussion

4.1. Annual sugarcane maps at the field scale over large spatial domains

Cropland field sizes vary a lot across the local, national and global scales, and in China smallholder farm system is the dominant form with average cropland field size less than one hectare (10,000 m²) (Samberg et al., 2016). Landsat images at 30-m spatial resolution have been used to map cropland distribution at the field scale (Gao et al., 2017) and the advantage of Landsat images for cropland mapping at the field scale were well documented (Loveland and Dwyer, 2012; Roy et al., 2014). As Sentinel-2 data at 10-m and 20-m spatial resolutions became freely

available since 2015, a number of studies have combined both Landsat and Sentinel-2 images to map croplands at the field scale (Defourny et al., 2019; Griffiths et al., 2019; Liu et al., 2020). In this study, we combined Landsat, Sentinel-2, and Sentinel-1 to identify and map croplands, cropping intensity and sugarcane at 10-m spatial resolution. In comparison to the studies that used only Landsat or Sentinel-2, the combined time series image data from LC/S2/S1 substantially increased the number of good-quality observations for field-scale agricultural applications, which addresses a critical data issue the land cover mapping community has faced in the past few years (Dong et al., 2015; Gong et al., 2013; Hansen et al., 2016).

In Guangxi, China, there is a period of rush-harvesting of early rice and rush-transplanting of late rice for the double paddy rice croplands (Fig. 4b). During this short period, which often lasts about two weeks, there is a high probability that because of clouds there is no good quality optical data to identify the flooding signals of paddy rice fields. Images acquired by SAR sensors are not affected by clouds and can be used for mapping surface waters and detecting flooding events in the cloud days (Bioresita et al., 2018). The Sentinel-1 VH backscatter signals are low when the land surfaces are covered by water (Fig. 4b, e). In this study, we used the Sentinel-1 VH data as an additional way to detect the water-related pixels in a year, which increases the accuracy of the water-related land cover map.

The phenological characteristics of sugarcane fields were

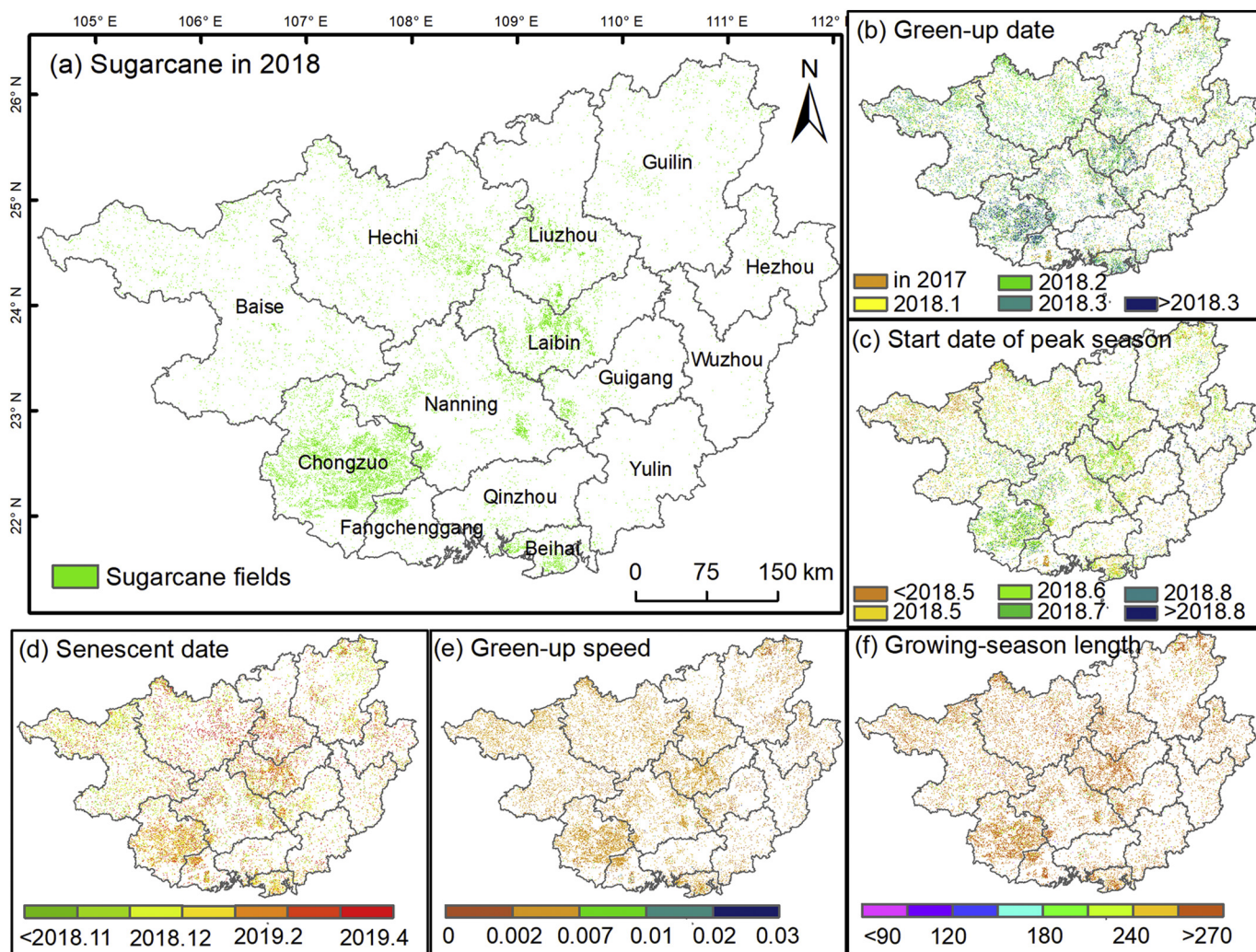


Fig. 8. (a) The sugarcane distribution map in 2018 for Guangxi, China. (b-f) show the distribution maps of phenology parameters of green-up date, start date of peak season, senescent date, green-up speed, and the length of growing season for the croplands having a single-cropping system. (For interpretation of the references to colour in this figure legend, the reader is referred to the web version of this article.)

recognized and used in previous studies of sugarcane mapping (Aguar et al., 2011; Baghdadi et al., 2011; Jiang et al., 2019a; Zhou et al., 2015). One study used time series Sentinel-1A images from 3/2017 to 2/2018 and the Random Forest algorithm to map sugarcane in

Zhanjiang city, Guangdong Province, China, and the resultant sugarcane map had an accuracy of 86.3% (Jiang et al., 2019a). Another study used multi-date Chinese HJ-1 CCD images (visible and near infrared bands; 30-m spatial resolution) from 6/2013 to 5/2014 to map

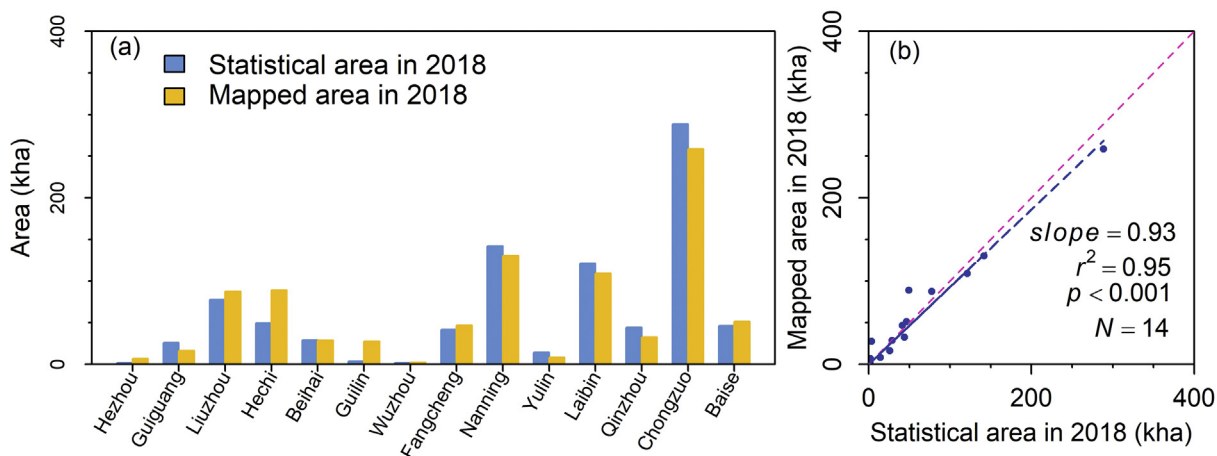


Fig. 9. A comparison of sugarcane area estimates by prefecture and city between the sugarcane map in 2018 and the agricultural statistical data reported for 2018. This comparison used the linear regression model of $y = a \cdot x$.

Table 3

Accuracy assessment of sugarcane map in 2018 based on the validation regions of interests (ROIs) from field photos, Google Earth images and Sentinel-2 images for sugarcane (SC) and other crops (OC). This table shows the User's (UA), Producer's (PA) and Overall (OA) accuracy with a 95% confidence interval. The validation samples are shown in Fig. S8.

		Reference			UA	PA	OA
		Sugarcane	Other crops	Total			
Map	Sugarcane	0.196	0.004	0.2	0.96 ± 0.005	0.88 ± 0.007	0.96 ± 0.002
	Other crops	0.022	0.778	0.8	0.97 ± 0.002	0.99 ± 0.001	
	Total	0.218	0.782				

sugarcane in Suixi county, Guangdong province, China, and the resultant sugarcane map had an overall accuracy of 93.6% (Zhou et al., 2015). In this study, we used the pixel- and phenology-based algorithms and time series LC/S2/S1 data, which substantially increased numbers of good-quality observations of individual pixels for better capturing phenological metrics of sugarcane fields. As a result, we generated an

accurate (96% overall accuracy) sugarcane map in 2018 at 10-m spatial resolution in Guangxi, China, and to our limited knowledge, it is the first sugarcane map at the field scale over the entire Guangxi province, which accounts for 65% of total sugarcane production in China (Tan et al., 2007).

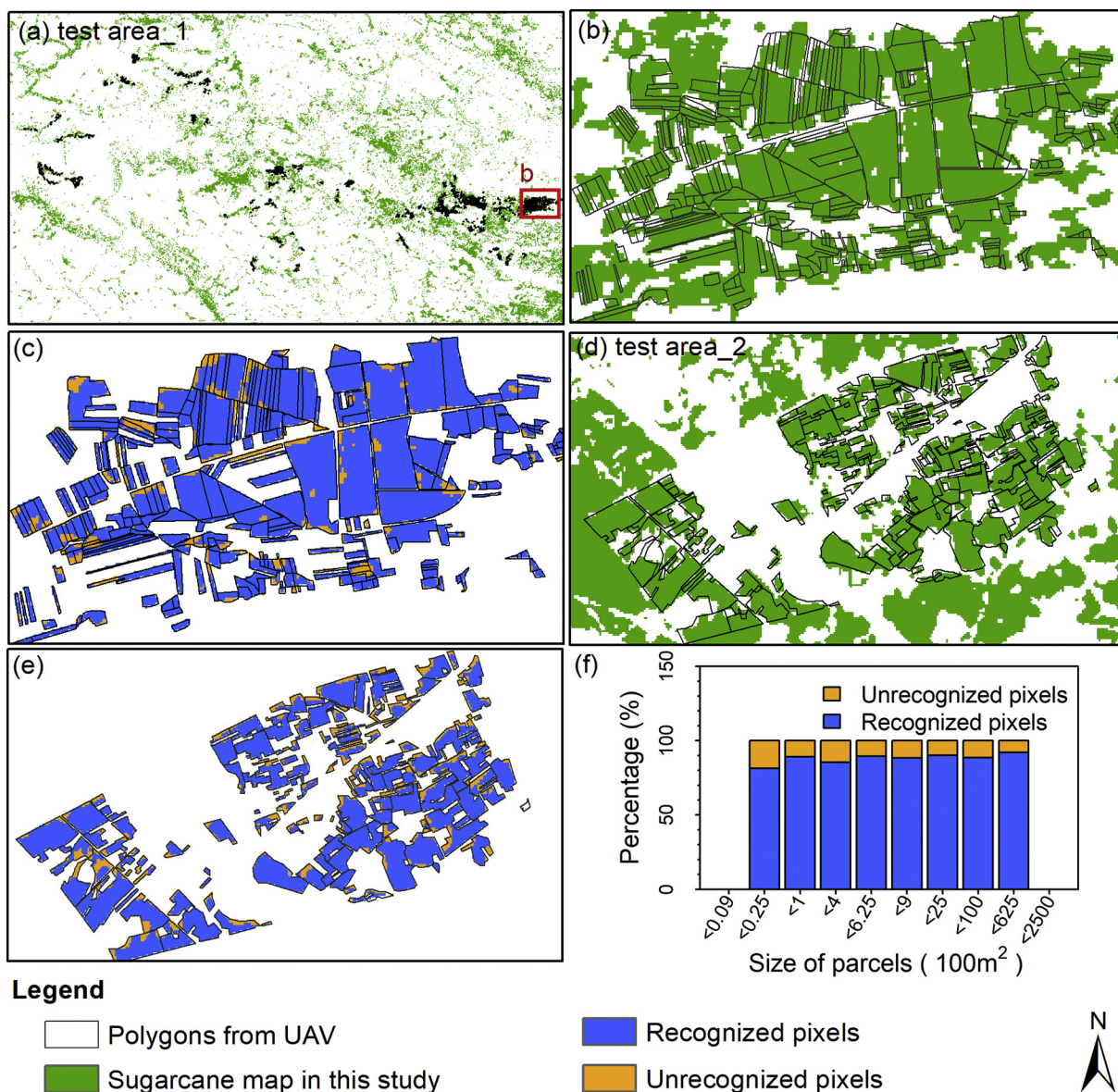


Fig. 10. (a, d) Spatial distribution of the small unmanned aerial system (sUAS) data at two pilot regions including 2249 and 139 polygons. Their locations in Guangxi, China are shown in Fig. S5. (b) a zoom-in view of the sUAS polygons in the first pilot region labeled as b in Fig. a. (c, e) the recognized and unrecognized pixels of the resultant sugarcane map in 2018 within each sUAS polygon for two pilot regions. (f) Proportions of recognized and unrecognized pixels with the changes of sugarcane field sizes.

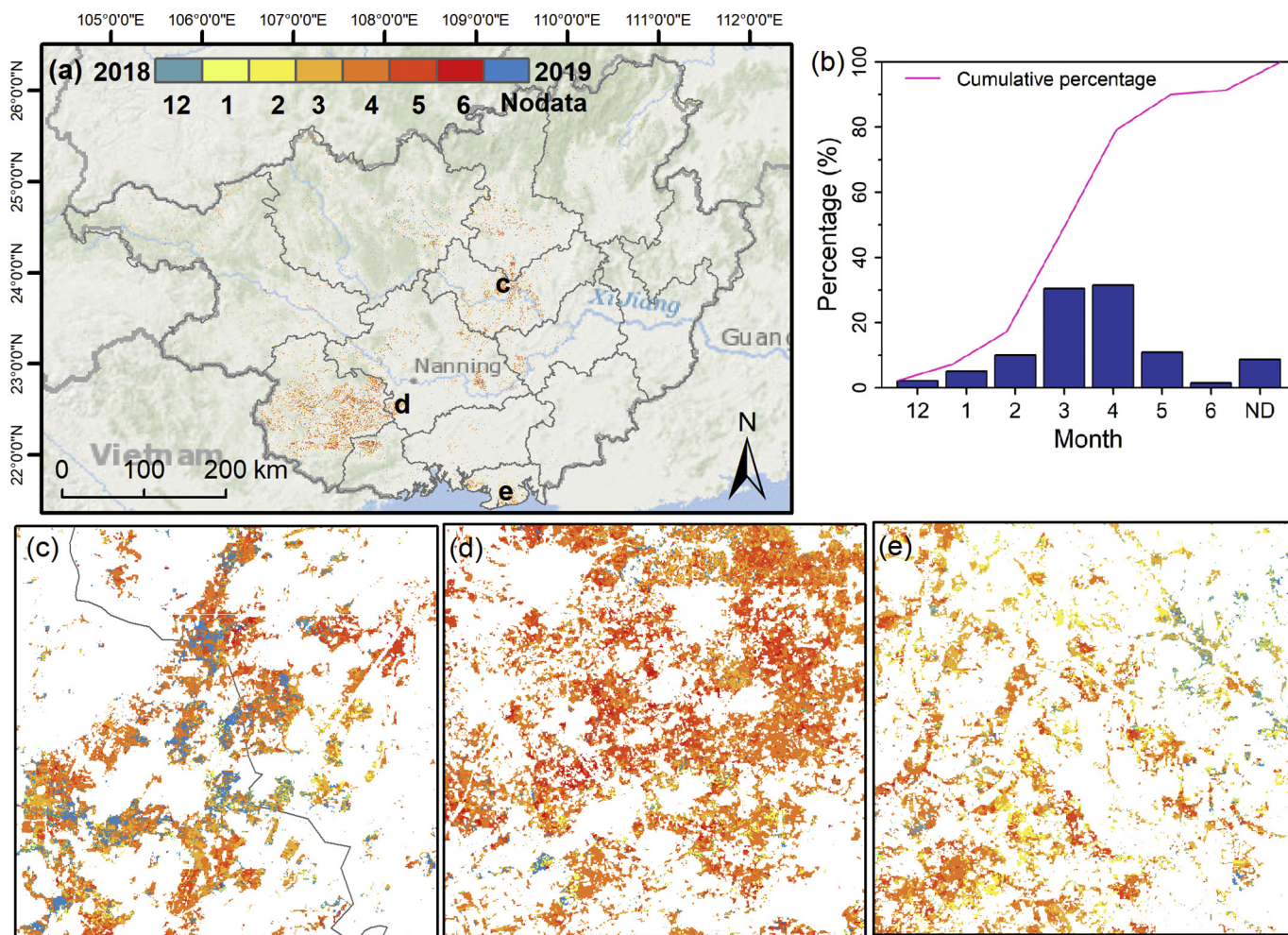


Fig. 11. (a) The green-up map of sugarcane fields in 2019. This is a monitoring work following the mapping of sugarcane fields in 2018 based on the Landsat/Sentinel-2 time series data. (b) the percentage of sugarcane field green up in each month from December 2018 to June 2019. (c-e) the zoom-in views for three random regions. Their locations are shown in (a). (For interpretation of the references to colour in this figure legend, the reader is referred to the web version of this article.)

4.2. Sources of errors in annual sugarcane maps at the field scale over large spatial domains

It has been a challenging task to generate annual maps of croplands and specific crop types at the field scale over large spatial domains (Jin et al., 2019; Luciano et al., 2019). Accuracy of annual sugarcane maps at the field scale is affected by several factors: (1) the definition of sugarcane fields (newly planted sugarcane field, ratooning sugarcane field), (2) types and number of satellite images, (3) training and validation datasets, (4) algorithms, (5) spatial resolution (scale) and spatial domains and (6) complexity of landscapes.

Topography affects the image data quality from both optical and microwave sensors, in particular over those areas with complex landscapes. Several studies used Landsat images to identify and map sugarcane fields in Brazil (Aguilar et al., 2011; Luciano et al., 2019; Luciano et al., 2018), where topography is simple and sugarcane fields are big, and the resultant sugarcane maps had high accuracy. In comparison, our study area (Guangxi province, China) has very complex and fragmented topography. In addition, most of sugarcane fields in Guangxi province are small. For Landsat images at 30-m spatial resolution, the number of mixed pixels of sugarcane fields and other land cover types could be large, which is one source of errors in the sugarcane map in 2018.

Both the top-of-atmosphere (TOA) reflectance and the surface reflectance (SR) images have been used for land cover mapping (Griffiths et al., 2019; Jin et al., 2019; Wang et al., 2019). We started to analyze

Sentinel-2 images in August 2019, at that time SR images from Sentinel-2 for 8/2017–7/2019 were not available in the Google Earth Engine. There is always a time lag (delay) between the TOA data and SR data. As we were trying to do in-season monitoring sugarcane fields, we used the TOA data from both Landsat and Sentinel-2 in this study, which is a source of errors in the sugarcane map in 2018. Future work is also needed to use time series SR images for sugarcane mapping.

Crops are developed in their favorable conditions resulting in diverse cropping seasons such as winter or summer cover crops (Torriani et al., 2007). We used four phenology metrics of GUD, SDPS, SD, and GUS as parameters to build the decision system for sugarcane crop mapping. The parameters of GUD and SD presents the start and end of the sugarcane growing season, which are varied among crops due to different thermal requirements of crops (Torriani et al., 2007; Zhong et al., 2011). SDPS indicates the start date of the peak season which corresponds to the rapid growth of sugarcane after tillering with full-canopy cover. GUS shows the growing speed in the rapid development period from the GUD to the SDPS. SDPS and GUS are variables to extract sugarcane crops using the middle segments of crop phenological development (Zhong et al., 2016a). To improve the classification approach for future works, we did a sensitivity analysis to evaluate the roles of these four parameters in the classification system (Fig. 12). We compared the changes of producer's (PA), user's (UA) and overall (OA) accuracies among sugarcane maps produced using four parameters (SC map) and without using the parameter of GUD (SC_no_GUD), GUS (SC_no_GUS), SDPS (SC_no_SDPS), and SD (SC_no_SD) (Fig. 12). The

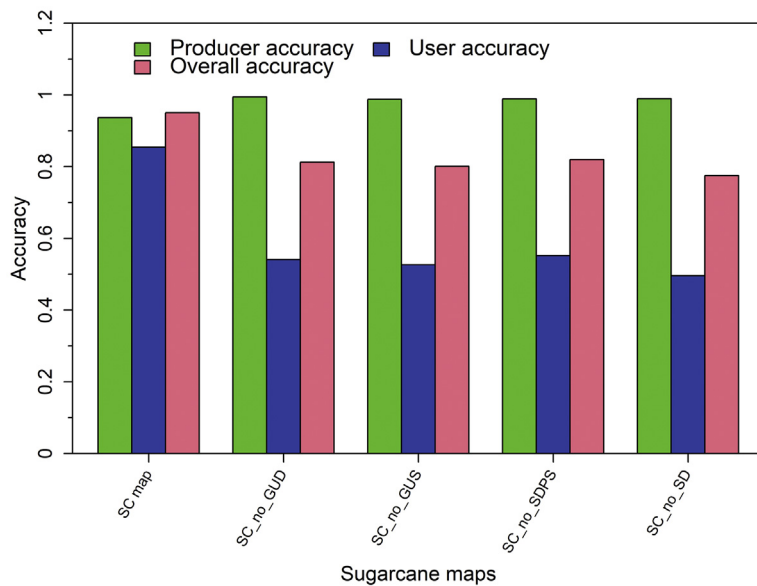


Fig. 12. Sensitivity analysis of phenology parameters for the sugarcane mapping. The producer's, user's and overall accuracies are used as indicators to compare the resultant sugarcane map (SC_map) and the sugarcane map without green-up date (SC_no_GUD), green-up speed (SC_no_GUS), start date of peak season (SC_no_SDPS), and senescent date (SC_no_SD) phenology parameters. (For interpretation of the references to colour in this figure legend, the reader is referred to the web version of this article.)

results demonstrated that these four parameters are all important to improve the user's accuracy and reduce the commission errors in the sugarcane mapping. Thus, the estimate qualities of these four parameters could be a source of errors in the resultant sugarcane map from the algorithm perspective.

4.3. Implications and improvements

The pixel- and phenology-based algorithm based on time series LC/S2/S1 images has the potential to map (1) sugarcane crop in other years, (2) sugarcane crop in other regions, and (3) other crop types. The classification rules were developed by selecting the unique phenology metrics of sugarcane crop. In a given area, the environmental factors, such as topography, climate, planting and management activities, for sugarcane cultivation are relatively consistent over normal years. Meanwhile, sugarcane is a ratoon crop with a long growing season from 8 months to more than one year (Luciano et al., 2018; Molijn et al., 2018). These features could result in the sugarcane crops planted in a same field continuously between years. Therefore, it is promising to use the proposed sugarcane mapping tool to map the sugarcane plantations in other years. With respect to the sugarcane mapping in other regions, this mapping tool can be applied by tuning the thresholds of the phenology parameters using the local training samples. It can address the potential differences in the phenology metrics of sugarcane crops under different environmental conditions. Furthermore, this sugarcane mapping tool could be applied to detect other crop types by revising the phenology metrics. It is supported by the previous studies on using phenology-based approaches to map various dominant crop types (e.g. paddy rice, winter wheat, maize, and soybean) at 30-m or coarser spatial resolutions (Chen et al., 2018b; Massey et al., 2017; Zhong et al., 2011). Currently, various machine learning and deep learning models are explored for crop classification (Jiang et al., 2019a; Luciano et al., 2019; Wang et al., 2019; Zhong et al., 2019). This sugarcane classification framework can be updated by integrating the phenology metrics and the machine learning models to map crop types in the future works.

In addition, to harmonize the images from different sensors, we applied the OLS regression coefficients to convert the TOA spectral reflectance from MSI to OLI. It is a fast and practical approach to construct consistent LC/S2 TOA time series at the GEE platform (Liu et al., 2020; Zhang et al., 2018). Recently, some other approaches have also been proposed to combine both sensors' data such as generating proxy values (Griffiths et al., 2019) and deep learning-based fusion (Shao et al., 2019). The deep learning-based fusion of LC/S2 has the

potential to adequately use the spatial information of Sentinel-2 to downscale the Landsat-8 images from 30-m to 10-m spatial resolution (Shao et al., 2019). With the development of the deep learning-based fusion network at the GEE platform, it will improve the LC/S2 blending time series images to develop crop mapping algorithms at the field scale over large spatial domains.

5. Conclusions

There is a need to map and monitor the spatial-temporal dynamics of sugarcane fields at the field scale over large spatial domains. In this study we developed a pixel- and phenology-based sugarcane mapping tool, which uses the time series optical images (Landsat, Sentinel-2A/B) and microwave images (Sentinel-1A/B) and the decision tree algorithms to identify and map croplands, cropping intensity (single, double and triple cropping in a year) and sugarcane. We generated an annual map of sugarcane fields in 2018 at 10-m spatial resolution in Guangxi, China, and the green-up dates of those sugarcane fields in 2019. This study shows that Landsat, Sentinel-2 and Sentinel-1 together may provide adequate numbers of good observations for sugarcane mapping in a study area with small crop fields and frequent cloud cover. The proposed pixel- and phenology-based sugarcane mapping tool has the potential to be applied for mapping sugarcane plantations in other years or other places in China. The resultant maps provide essential information for sugarcane crop management and impact studies on economics and the environment.

Declaration of Competing Interest

The authors declare that they have no known competing financial interests or personal relationships that could have appeared to influence the work reported in this paper.

Acknowledgements

This study was supported in part by research grants from NASA Land Use and Land Cover Change program (grant no. NNX14AD78G) and USDA NIFA (2020-67104-30935). We thank Dr. Paul M White from the USDA-ARS Sugarcane Research Unit, Houma, LA, USA for his comments and English editing of the manuscript. We thank three anonymous reviewers for their time and effort in reviewing the manuscript.

Appendix A. Supplementary data

Supplementary data to this article can be found online at <https://doi.org/10.1016/j.rse.2020.111951>.

References

- Aguilar, D.A., Rudorff, B.F.T., Silva, W.F., Adami, M., Mello, M.P., 2011. Remote sensing images in support of environmental protocol: monitoring the sugarcane harvest in Sao Paulo state, Brazil. *Remote Sens.* 3, 2682–2703.
- Baghdadi, N., Todoroff, P., Zribi, M., 2011. Multitemporal observations of sugarcane by TerraSAR-X sensor. In: 2011 IEEE International Geoscience and Remote Sensing Symposium, pp. 1401–1404.
- Bargiel, D., 2017. A new method for crop classification combining time series of radar images and crop phenology information. *Remote Sens. Environ.* 198, 369–383.
- Begue, A., Arvor, D., Bellon, B., Betbeder, J., de Abelleira, D., Ferraz, R.P.D., Lebourgeois, V., Lelong, C., Simoes, M., Veron, S.R., 2018. Remote sensing and cropping practices: a review. *Remote Sens.* 10.
- Bioresita, F., Puissant, A., Stumpf, A., Malet, J.-P., 2018. A method for automatic and rapid mapping of water surfaces from sentinel-1 imagery. *Remote Sens.* 10, 217.
- Cardona, C.A., Quintero, J.A., Paz, I.C., 2010. Production of bioethanol from sugarcane bagasse: status and perspectives. *Bioresour. Technol.* 101, 4754–4766.
- Chen, J.S., Huang, J.X., Hu, J.X., 2011. Mapping rice planting areas in southern China using the China environment satellite data. *Math. Comput. Model.* 54, 1037–1043.
- Chen, B.Q., Xiao, X.M., Ye, H.C., Ma, J., Doughty, R., Li, X.P., Zhao, B., Wu, Z.X., Sun, R., Dong, J.W., Qin, Y.W., Xie, G.S., 2018a. Mapping Forest and their spatial-temporal changes from 2007 to 2015 in tropical Hainan Island by integrating ALOS/TMOS-2 L-band SAR and Landsat optical images. *IEEE J. Sel. Top. Appl. Earth Observ. Remote Sensing* 11, 852–867.
- Chen, Y.L., Lu, D.S., Moran, E., Batistella, M., Dutra, L.V., Sanches, I.D., da Silva, R.F.B., Huang, J.F., Luiz, A.J.B., de Oliveira, M.A.F., 2018b. Mapping croplands, cropping patterns, and crop types using MODIS time-series data. *Int. J. Appl. Earth Obs. Geoinf.* 69, 133–147.
- Defante, L.R., Vilpoux, O.F., Sauer, L., 2018. Rapid expansion of sugarcane crop for biofuels and influence on food production in the first producing region of Brazil. *Food Policy* 79, 121–131.
- Defourny, P., Bontemps, S., Bellemans, N., Cara, C., Dedieu, G., Guzzonato, E., Hagolle, O., Inglada, J., Nicola, L., Rabaute, T., Savinaud, M., Udroui, C., Valero, S., Bégué, A., Dejoux, J.-F., El Harti, A., Ezzahar, J., Kussul, N., Labbassi, K., Lebourgeois, V., Miao, Z., Newby, T., Nyamugama, A., Salh, N., Shelestov, A., Simonneaux, V., Traore, P.S., Traore, S.S., Koetz, B., 2019. Near real-time agriculture monitoring at national scale at parcel resolution: performance assessment of the Sen2-Agri automated system in various cropping systems around the world. *Remote Sens. Environ.* 221, 551–568.
- Defries, R.S., Townshend, J.R.G., 1994. Nvdi-derived land-cover classifications at a global-scale. *Int. J. Remote Sens.* 15, 3567–3586.
- Di Vittorio, C.A., Georgakakos, A.P., 2018. Land cover classification and wetland inundation mapping using MODIS. *Remote Sens. Environ.* 204, 1–17.
- Dong, J.W., Xiao, X.M., Kou, W.L., Qin, Y.W., Zhang, G.L., Li, L., Jin, C., Zhou, Y.T., Wang, J., Biradar, C., Liu, J.Y., Moore, B., 2015. Tracking the dynamics of paddy rice planting area in 1986–2010 through time series Landsat images and phenology-based algorithms. *Remote Sens. Environ.* 160, 99–113.
- El Hajj, M., Begue, A., Guillaume, S., Martine, J.F., 2009. Integrating SPOT-5 time series, crop growth modeling and expert knowledge for monitoring agricultural practices - the case of sugarcane harvest on Reunion Island. *Remote Sens. Environ.* 113, 2052–2061.
- Fischer, G., Shah, M., van Velthuizen, H., Nachtergaele, F.O., 2001. Global Agro-Ecological Assessment for Agriculture in the 21st Century.
- Galford, G.L., Mustard, J.F., Melillo, J., Gendrin, A., Cerri, C.C., Cerri, C.E.P., 2008. Wavelet analysis of MODIS time series to detect expansion and intensification of row-crop agriculture in Brazil. *Remote Sens. Environ.* 112, 576–587.
- Gao, F., Anderson, M.C., Zhang, X., Yang, Z., Alfieri, J.G., Kustas, W.P., Mueller, R., Johnson, D.M., Prueger, J.H., 2017. Toward mapping crop progress at field scales through fusion of Landsat and MODIS imagery. *Remote Sens. Environ.* 188, 9–25.
- Gong, P., Wang, J., Yu, L., Zhao, Y.C., Zhao, Y.Y., Liang, L., Niu, Z.G., Huang, X.M., Fu, H.H., Liu, S., Li, C.C., Li, X.Y., Fu, W., Liu, C.X., Xu, Y., Wang, X.Y., Cheng, Q., Hu, L.Y., Yao, W.B., Zhang, H., Zhu, P., Zhao, Z.Y., Zhang, H.Y., Zheng, Y.M., Ji, L.Y., Zhang, Y.W., Chen, H., Yan, A., Guo, J.H., Yu, L., Wang, L., Liu, X.J., Shi, T.T., Zhu, M.H., Chen, Y.L., Yang, G.W., Tang, P., Xu, B., Giri, C., Clinton, N., Zhu, Z.L., Chen, J., Chen, J., 2013. Finer resolution observation and monitoring of global land cover: first mapping results with Landsat TM and ETM+ data. *Int. J. Remote Sens.* 34, 2607–2654.
- Griffiths, P., Nendel, C., Hostert, P., 2019. Intra-annual reflectance composites from Sentinel-2 and Landsat for national-scale crop and land cover mapping. *Remote Sens. Environ.* 220, 135–151.
- Hansen, M.C., Potapov, P.V., Goetz, S.J., Turubanova, S., Tyukavina, A., Krylov, A., Kommareddy, A., Egorov, A., 2016. Mapping tree height distributions in sub-Saharan Africa using Landsat 7 and 8 data. *Remote Sens. Environ.* 185, 221–232.
- Henry, F., Herwindiati, D.E., Mulyono, S., Hendryli, J., 2017. Sugarcane land classification with satellite imagery using logistic regression model. In: IOP Conference Series: Materials Science and Engineering. IOP Publishing p. 012024.
- Hu, S., Shi, L.S., Huang, K., Zha, Y.Y., Hu, X.L., Ye, H., Yang, Q., 2019. Improvement of sugarcane crop simulation by SWAP-WOFOST model via data assimilation. *Field Crop Res.* 232, 49–61.
- Huete, A., Didan, K., Miura, T., Rodriguez, E.P., Gao, X., Ferreira, L.G., 2002. Overview of the radiometric and biophysical performance of the MODIS vegetation indices. *Remote Sens. Environ.* 83, 195–213.
- Hurni, K., Schneider, A., Heinemann, A., Nong, D.H., Fox, J., 2017. Mapping the expansion of boom crops in mainland Southeast Asia using dense time stacks of Landsat data. *Remote Sens.* 9.
- Jackson, T.J., Chen, D.Y., Cosh, M., Li, F.Q., Anderson, M., Walthall, C., Doriaswamy, P., Hunt, E.R., 2004. Vegetation water content mapping using Landsat data derived normalized difference water index for corn and soybeans. *Remote Sens. Environ.* 92, 475–482.
- Jiang, H., Li, D., Jing, W.L., Xu, J.H., Huang, J.X., Yang, J., Chen, S.S., 2019a. Early season mapping of sugarcane by applying machine learning algorithms to sentinel-1A/2 time series data: a case study in Zhanjiang City, China. *Remote Sens.* 11.
- Jiang, M., Xin, L., Li, X., Tan, M., Wang, R., 2019b. Decreasing Rice cropping intensity in southern China from 1990 to 2015. *Remote Sens.* 11, 35.
- Jin, Z.N., Azzari, G., You, C., Di Tommaso, S., Aston, S., Burke, M., Lobell, D.B., 2019. Smallholder maize area and yield mapping at national scales with Google earth engine. *Remote Sens. Environ.* 228, 115–128.
- Johnson, B.A., Scheyvens, H., Shivakoti, B.R., 2014. An ensemble pansharpening approach for finer-scale mapping of sugarcane with Landsat 8 imagery. *Int. J. Appl. Earth Obs. Geoinf.* 33, 218–225.
- Jonsson, P., Eklundh, L., 2004. TIMESAT - a program for analyzing time-series of satellite sensor data. *Comput. Geosci.* 30, 833–845.
- Li, L., Friedl, M.A., Xin, Q.C., Gray, J., Pan, Y.Z., Frothing, S., 2014. Mapping crop cycles in China using MODIS-EVI time series. *Remote Sens.* 6, 2473–2493.
- Lin, H., Chen, J., Pei, Z., Zhang, S., Hu, X., 2009. Monitoring sugarcane growth using ENVISAT ASAR data. *IEEE Trans. Geosci. Remote Sens.* 47, 2572–2580.
- Liu, L., Xiao, X., Qin, Y., Wang, J., Xu, X., Hu, Y., Qiao, Z., 2020. Mapping cropping intensity in China using time series Landsat and Sentinel-2 images and Google earth engine. *Remote Sens. Environ.* 239, 111624.
- Loveland, T.R., Dwyer, J.L., 2012. Landsat: building a strong future. *Remote Sens. Environ.* 122, 22–29.
- Luciano, A.C.D.S., Picoli, M.C.A., Rocha, J.V., Franco, H.C.J., Sanches, G.M., Leal, M.R.L.V., le Maire, G., 2018. Generalized space-time classifiers for monitoring sugarcane areas in Brazil. *Remote Sens. Environ.* 215, 438–451.
- Luciano, A.C.D., Picoli, M.C.A., Rocha, J.V., Duft, D.G., Lamparelli, R.A.C., Leal, M.R.L.V., Le Maire, G., 2019. A generalized space-time OBIA classification scheme to map sugarcane areas at regional scale, using Landsat images time-series and the random forest algorithm. *Int. J. Appl. Earth Obs. Geoinf.* 80, 127–136.
- Massey, R., Sankey, T.T., Congalton, R.G., Yadav, K., Thenkabail, P.S., Ozdogan, M., Meador, A.J.S., 2017. MODIS phenology-derived, multi-year distribution of continuous US crop types. *Remote Sens. Environ.* 198, 490–503.
- Meng, E.C., 2006. Maize in China: Production Systems, Constraints, and Research Priorities. Cimmyt.
- Molijn, R.A., Iannini, L., Rocha, J.V., Hanssen, R.F., 2018. Ground reference data for sugarcane biomass estimation in São Paulo state, Brazil. *Scientific Data* 5, 180150.
- Moore, P.H., Botha, F.C., 2013. Sugarcane: Physiology, Biochemistry and Functional Biology. John Wiley & Sons.
- Mulianga, B., Begue, A., Clouvel, P., Todoroff, P., 2015. Mapping cropping practices of a sugarcane-based cropping system in Kenya using remote sensing. *Remote Sensing* 7, 14428–14444.
- Olofsson, P., Foody, G.M., Herold, M., Stehman, S.V., Woodcock, C.E., Wulder, M.A., 2014. Good practices for estimating area and assessing accuracy of land change. *Remote Sens. Environ.* 148, 42–57.
- Pena-Barragan, J.M., Ngugi, M.K., Plant, R.E., Six, J., 2011. Object-based crop identification using multiple vegetation indices, textural features and crop phenology. *Remote Sens. Environ.* 115, 1301–1316.
- Qin, Y., Xiao, X., Dong, J., Chen, B., Liu, F., Zhang, G., Zhang, Y., Wang, J., Wu, X., 2017a. Quantifying annual changes in built-up area in complex urban-rural landscapes from analyses of PALSAR and Landsat images. *ISPRS J. Photogramm. Remote Sens.* 124, 89–105.
- Qin, Y.W., Xiao, X.M., Dong, J.W., Zhou, Y.T., Wang, J., Doughty, R.B., Chen, Y., Zou, Z.H., Moore, B., 2017b. Annual dynamics of forest areas in South America during 2007–2010 at 50m spatial resolution. *Remote Sens. Environ.* 201, 73–87.
- Qin, Y.W., Xiao, X.M., Dong, J.W., Zhang, Y., Wu, X.C., Shimabukuro, Y., Arai, E., Biradar, C., Wang, J., Zou, Z.H., Liu, F., Shi, Z., Doughty, R., Moore, B., 2019. Improved estimates of forest cover and loss in the Brazilian Amazon in 2000–2017. *Nat. Sustain.* 2, 764–772.
- Qiu, B.W., Luo, Y.H., Tang, Z.H., Chen, C.C., Lu, D.F., Huang, H.Y., Chen, Y.Z., Chen, N., Xu, W.M., 2017. Winter wheat mapping combining variations before and after estimated heading dates. *ISPRS J. Photogramm. Remote Sens.* 123, 35–46.
- Roy, D.P., Wulder, M.A., Loveland, T.R., Woodcock, C.E., Allen, R.G., Anderson, M.C., Helder, D., Irons, J.R., Johnson, D.M., Kennedy, R., Scambos, T., Schaaf, C.B., Schott, J.R., Sheng, Y., Vermote, E.F., Belward, A.S., Bindschadler, R., Cohen, W.B., Gao, F., Hipple, J.D., Hostert, P., Huntington, J., Justice, C.O., Kilic, A., Kovalsky, V., Lee, Z.P., Lymburner, L., Masek, J.G., McCorkel, J., Shuai, Y., Trezza, R., Vogelmann, J., Wynne, R.H., Zhu, Z., 2014. Landsat-8: science and product vision for terrestrial global change research. *Remote Sens. Environ.* 145, 154–172.
- Roy, D.P., Kovalsky, V., Zhang, H.K., Vermote, E.F., Yan, L., Kumar, S.S., Egorov, A., 2016. Characterization of Landsat-7 to Landsat-8 reflective wavelength and normalized difference vegetation index continuity. *Remote Sens. Environ.* 185, 57–70.
- Rudorff, B.F.T., de Aguiar, D.A., da Silva, W.F., Sugawara, L.M., Adami, M., Moreira, M.A., 2010. Studies on the rapid expansion of sugarcane for ethanol production in Sao Paulo state (Brazil) using Landsat data. *Remote Sens.* 2, 1057–1076.
- Samberg, L.H., Gerber, J.S., Ramankutty, N., Herrero, M., West, P.C., 2016. Subnational distribution of average farm size and smallholder contributions to global food production. *Environ. Res. Lett.* 11.

- Shao, Z.F., Cai, J.J., Fu, P., Hu, L.Q., Liu, T., 2019. Deep learning-based fusion of Landsat-8 and Sentinel-2 images for a harmonized surface reflectance product. *Remote Sens. Environ.* 235.
- Shield, I., 2016. 11 - sugar and starch crop supply chains. In: Holm-Nielsen, J.B., Ehimen, E.A. (Eds.), *Biomass Supply Chains for Bioenergy and Biorefining*. Woodhead Publishing, pp. 249–269.
- Sidike, P., Sagan, V., Maimaitijiang, M., Maimaitiyiming, M., Shakoore, N., Burken, J., Mockler, T., Fritschi, F.B., 2019. dPEN: deep progressively expanded network for mapping heterogeneous agricultural landscape using WorldView-3 satellite imagery. *Remote Sens. Environ.* 221, 756–772.
- Silalertruksa, T., Gheewala, S.H., 2018. Land-water-energy nexus of sugarcane production in Thailand. *J. Clean. Prod.* 182, 521–528.
- Sindhu, R., Gnansounou, E., Binod, P., Pandey, A., 2016. Bioconversion of sugarcane crop residue for value added products - an overview. *Renew. Energy* 98, 203–215.
- Song, Y., Wang, J., 2019. Mapping winter wheat planting area and monitoring its phenology using Sentinel-1 backscatter time series. *Remote Sens.* 11.
- Tan, Z., Wu, L., Ding, M., Yang, X., Ou, Z., He, Y., Kuang, Z., 2007. Study on the extraction of sugar-cane planting areas from EOS/MODIS data. *Meteorological Monthly* 33, 76–81.
- Torriani, D.S., Calanca, P., Schmid, S., Beniston, M., Fuhrer, J., 2007. Potential effects of changes in mean climate and climate variability on the yield of winter and spring crops in Switzerland. *Clim. Res.* 34, 59–69.
- Tucker, C.J., 1979. Red and photographic infrared linear combinations for monitoring vegetation. *Remote Sens. Environ.* 8, 127–150.
- Verma, A.K., Garg, P.K., Prasad, K.S.H., 2017. Sugarcane crop identification from LISS IV data using ISODATA, MLC, and indices based decision tree approach. *Arab. J. Geosci.* 10.
- Vieira, M.A., Formaggio, A.R., Renno, C.D., Atzberger, C., Aguiar, D.A., Mello, M.P., 2012. Object based image analysis and data mining applied to a remotely sensed Landsat time-series to map sugarcane over large areas. *Remote Sens. Environ.* 123, 553–562.
- Vinod, K.V.K., Kamal, J., 2010. Development of spectral signatures and classification of sugarcane using ASTER data. *Int. J. Comp. Sci. Commun.* 1, 245–251.
- Wang, J., Huang, J., Wang, L., Hu, Y., Han, P., Huang, W., 2014. Identification of sugarcane based on object-oriented analysis using time-series HJ CCD data. *Trans. Chin. Soc. Agric. Eng.* 30, 145–151.
- Wang, J., Xiao, X., Qin, Y., Doughty, R.B., Dong, J., Zou, Z., 2018a. Characterizing the encroachment of juniper forests into sub-humid and semi-arid prairies from 1984 to 2010 using PALSAR and Landsat data. *Remote Sens. Environ.* 205, 166–179.
- Wang, L.H., Tian, F., Wang, Y.H., Wu, Z.D., Schurgers, G., Fensholt, R., 2018b. Acceleration of global vegetation Greenup from combined effects of climate change and human land management. *Glob. Chang. Biol.* 24, 5484–5499.
- Wang, S., Azzari, G., Lobell, D.B., 2019. Crop type mapping without field-level labels: random forest transfer and unsupervised clustering techniques. *Remote Sens. Environ.* 222, 303–317.
- Wardlow, B.D., Egbert, S.L., Kastens, J.H., 2007. Analysis of time-series MODIS 250 m vegetation index data for crop classification in the US central Great Plains. *Remote Sens. Environ.* 108, 290–310.
- Xavier, A.C., Rudorff, B.F.T., Berka, L.M.S., Moreira, M.A., 2006. Multi-temporal analysis of MODIS data to classify sugarcane crop. *Int. J. Remote Sens.* 27, 755–768.
- Xiao, X.M., Boles, S., Liu, J.Y., Zhuang, D.F., Frolking, S., Li, C.S., Salas, W., Moore, B., 2005. Mapping paddy rice agriculture in southern China using multi-temporal MODIS images. *Remote Sens. Environ.* 95, 480–492.
- Xiao, X.M., Boles, S., Frolking, S., Li, C.S., Babu, J.Y., Salas, W., Moore, B., 2006. Mapping paddy rice agriculture in south and Southeast Asia using multi-temporal MODIS images. *Remote Sens. Environ.* 100, 95–113.
- Xiao, X., Biradar, C.M., Czarnecki, C., Alabi, T., Keller, M., 2009. A simple algorithm for large-scale mapping of Evergreen forests in tropical America, Africa and Asia. *Remote Sens.* 1, 355–374.
- Xu, H., 2006. Modification of normalised difference water index (NDWI) to enhance open water features in remotely sensed imagery. *Int. J. Remote Sens.* 27, 3025–3033.
- Zhang, B.-Q., Yang, L.-T., Li, Y.-R., 2015. Physiological and biochemical characteristics related to cold resistance in sugarcane. *Sugar Tech* 17, 49–58.
- Zhang, G., Xiao, X., Biradar, C.M., Dong, J., Qin, Y., Menarguez, M.A., Zhou, Y., Zhang, Y., Jin, C., Wang, J., Doughty, R.B., Ding, M., Moore III, B., 2017. Spatiotemporal patterns of paddy rice croplands in China and India from 2000 to 2015. *Sci. Total Environ.* 579, 82–92.
- Zhang, H.K., Roy, D.P., Yan, L., Li, Z., Huang, H., Vermote, E., Skakun, S., Roger, J.-C., 2018. Characterization of sentinel-2A and Landsat-8 top of atmosphere, surface, and nadir BRDF adjusted reflectance and NDVI differences. *Remote Sens. Environ.* 215, 482–494.
- Zhong, L., Hawkins, T., Biging, G., Gong, P., 2011. A phenology-based approach to map crop types in the San Joaquin Valley, California. *Int. J. Remote Sens.* 32, 7777–7804.
- Zhong, L.H., Gong, P., Biging, G.S., 2014. Efficient corn and soybean mapping with temporal extendability: a multi-year experiment using Landsat imagery. *Remote Sens. Environ.* 140, 1–13.
- Zhong, L., Hu, L., Yu, L., Gong, P., Biging, G.S., 2016a. Automated mapping of soybean and corn using phenology. *ISPRS J. Photogramm. Remote Sens.* 119, 151–164.
- Zhong, L.H., Hu, L.N., Yu, L., Gong, P., Biging, G.S., 2016b. Automated mapping of soybean and corn using phenology. *ISPRS J. Photogramm. Remote Sens.* 119, 151–164.
- Zhong, L.H., Hu, L.N., Zhou, H., 2019. Deep learning based multi-temporal crop classification. *Remote Sens. Environ.* 221, 430–443.
- Zhou, Z., Huang, J.F., Wang, J., Zhang, K.Y., Kuang, Z.M., Zhong, S.Q., Song, X.D., 2015. Object-oriented classification of sugarcane using time-series middle-resolution remote sensing data based on AdaBoost. *PLoS One* 10.
- Zhu, Z., Woodcock, C.E., 2012. Object-based cloud and cloud shadow detection in Landsat imagery. *Remote Sens. Environ.* 118, 83–94.
- Zou, Z.H., Xiao, X.M., Dong, J.W., Qin, Y.W., Doughty, R.B., Menarguez, M.A., Zhang, G.L., Wang, J., 2018. Divergent trends of open-surface water body area in the contiguous United States from 1984 to 2016. *Proc. Natl. Acad. Sci. U. S. A.* 115, 3810–3815.